Article

Snap inflatable modular metastructures for multipath, multimode morphing machines

Graphical abstract
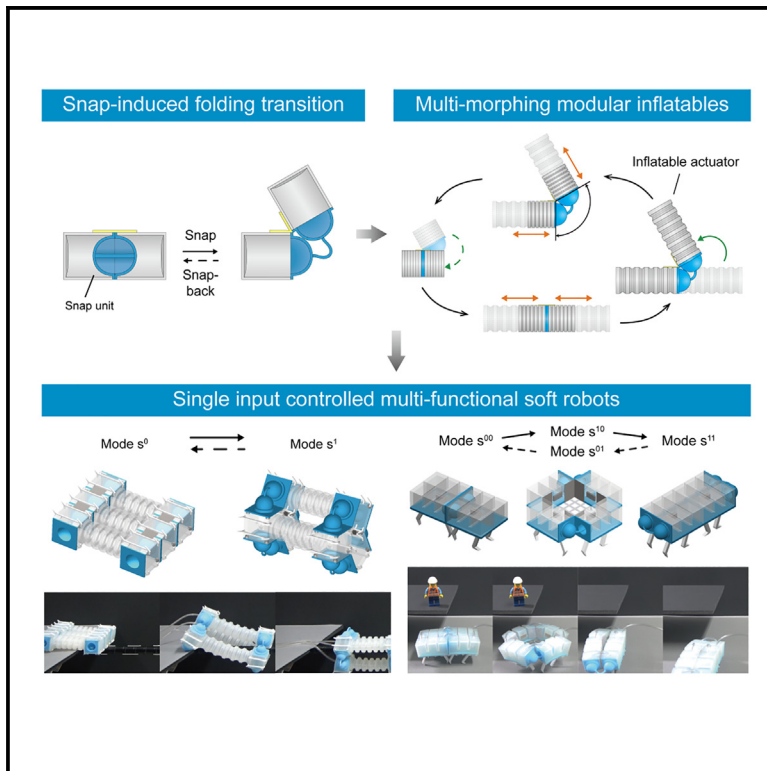
Authors

Ji-Sung Park, Kanghyun Ki, Anna Lee, Jeong-Yun Sun, Ho-Young Kim

Correspondence

annalee@postech.ac.kr (A.L.),
jysun@snu.ac.kr (J.-Y.S.),
hyk@snu.ac.kr (H.-Y.K.)

In brief

Park et al. present a design strategy leveraging snap-through folding and modular assemblies to achieve reconfigurable morphing mechanisms. By integrating discrete snapping transitions with continuous pneumatic actuation, their work enables modular robots to perform complex transitions and functionalities using a single input control, demonstrating potential applications in soft, adaptive devices.

Highlights

- Modular assembly of snapping units enables versatile morphing through snap-folding

- Snap transitions combined with continuous actuation enable multifunctionality

- Origami- and kirigami-inspired modular designs enhance reconfigurability

- Potential applications for soft robotic systems are demonstrated

CellPress

Article

Snap inflatable modular metastructures for multipath, multimode morphing machines

Ji-Sung Park,[1] Kanghyun Ki,[2] Anna Lee,[2,*] Jeong-Yun Sun,[3,4,*] and Ho-Young Kim[1,5,6,*]

[1]Department of Mechanical Engineering, Seoul National University, Seoul 08826, Korea
[2]Department of Mechanical Engineering, Pohang University of Science and Technology, Pohang 37673, Korea
[3]Department of Materials Science and Engineering, Seoul National University, Seoul 08826, Korea
[4]Research Institute of Advanced Materials, Seoul National University, Seoul 08826, Korea
[5]Institute of Advanced Machines and Design, Seoul National University, Seoul 08826, Korea
[6]Lead contact
*Correspondence: annalee@postech.ac.kr (A.L.), jysun@snu.ac.kr (J.-Y.S.), hyk@snu.ac.kr (H.-Y.K.)
https://doi.org/10.1016/j.xcrp.2025.102448

SUMMARY

The practical success of soft robotics depends largely on actuators with advanced shape-morphing capabilities for tasks such as dexterous manipulation and adaptive locomotion. Traditional soft machines have faced limitations caused by the complexity of managing multiple operational modes within a single device. To address this, we introduce highly adaptable morphing machines that combine modular origami and kirigami designs with pneumatic snap-through and snap-back of bistable shells at tile junctions or kirigami creases. Controlled pressure triggers selective snapping at creases, enabling programmed shape transformations along multiple paths. Our analytical and computational framework predicts system morphology and dynamics, guiding the design of snap inflatable modular metastructures (SIMMs). Utilizing SIMMs, we have developed soft robots capable of navigating diverse terrains and performing multifunctional tasks, demonstrated by "3D spinning ball" and "2D quad-tessellation" modes. This research advances morphing capabilities from a single input source, opening new possibilities for applications including minimally invasive surgery and search and rescue.

INTRODUCTION

Soft actuators capable of flexible interaction with complex environments have recently drawn great interest as a viable solution to perform functions previously unachievable by conventional rigid robots.[1] Drastic shape morphing of soft bodies opens a wide range of new functionalities including manipulation of arbitrary objects[2–6] and locomotion through harsh environments.[7–12] However, the full potential of these soft systems is yet to be realized, as the complexity of actuation and control introduces significant challenges. Increased functionality in soft robotics often requires complex combination of mechanisms and actuations dedicated for each specific motion.[13–15] This approach not only escalates the complexity of the design but also imposes dependency on additional, typically rigid, components that can hinder the system's flexibility. Auxiliary rigid components for precise control, such as regulators and valves, underscore a pivotal restraint in exploiting the inherent compliance of these soft elements, ultimately limiting their adaptability and functional versatility.[16] As a consequence, there is a pressing need for innovations that facilitate multimorphing capabilities without employing the rigid control elements. Simplifying the design to reduce rigid parts also decreases the overall system weight, volume, cost, and complexity. Recent attempts to increase the number of actuation modes per input control in pneumatic actuators,

such as the deploy-stretch mechanism,[17] the time lag effect via viscous flow,[18] and the strain-hardening effect,[19] have been limited to relatively simple sequential morphing and thus incapable of multipath actuation and control of each mode.

Among numerous programmable structures, one approach to overcome such difficulties is by utilizing the concept of origami or kirigami.[10,11,17,20–24] Through precise patterns of folding and cutting, origami and kirigami provide ways to attain desired topologies and mechanical behaviors by concentrating the deformation in the creases and cuts (flexible) rather than the planar areas (relatively stiff) of the material.[25] Furthermore, the intrinsic adaptability of hybrid ori-kirigami designs is emerging as a promising strategy for advanced tasks that require both softness and sufficient rigidity of the system.[26] Recent advances in modular origami metastructures have successfully demonstrated shape-morphing capabilities through the use of assembled modules.[27] However, these systems still rely on multiple onboard rigid, electric motors for actuation and control, which limits the versatility and potential applications of origami and kirigami designs.[28]

While a large number of soft machines activated by chemical, thermal, and electromagnetic stimuli have been studied, pneumatic or hydraulic actuators have proven to be useful for applications requiring strong, scalable, and rapid actuation.[9,29] Inflatable actuators are commonly used for expansion, contraction,
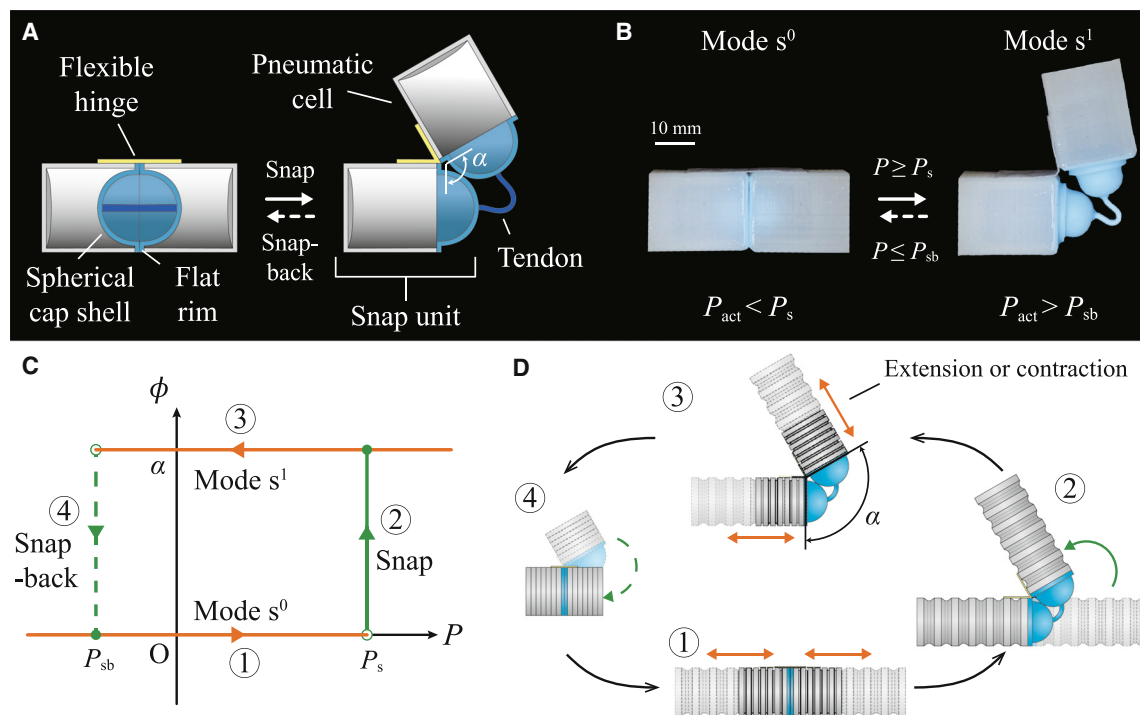
Figure 1. SIMM with multimorphing capability

(A) Schematic illustration and (B) experimental image of a snap unit and a SIMM activated by pressure.

(C) The folding angle-pressure ($\phi - P$) diagram and (D) the corresponding illustration of hysteretic transition cycle of the SIMM combined with bellows-shaped extension actuator. Green solid and dashed lines correspond to snap-through folding and snap-back unfolding procedures, respectively. Orange solid lines correspond to continuous extension and contraction actuations in each state.

bending or twisting, and combinations of these modes.[30] While these actuators primarily achieve motions through gradual and continuous deformation upon the supply of pressure, the recent advancements in soft pneumatic systems exploit nonlinearities associated with buckling or snapping instability, enabling rapid shape-shifting.[4,9,23,31–37] Furthermore, snap-through buckling elements often grant multistability to the system by connecting two or more bistable units and then independently triggering the instability of each unit.[38] Such multiple equilibrium states provide a solution to the problem of pneumatic systems continuously consuming power to maintain their deformed structure.[23,39–42]

In this work, inspired by modular origami and kirigami design principles and multistable structures, we introduce a snap inflatable modular metastructure (SIMM) mechanism that achieves multiple reversible modes with a single pressure input. While traditional origami and kirigami principles involve cutting and folding thin sheets, our approach adapts these concepts to three-dimensional, pneumatically actuated structures. This innovative approach significantly reduces the system's physical complexity by minimizing reliance on auxiliary rigid components such as valves and mechanical connectors, which are typically essential for multifunctionality in traditional systems. By simplifying the hardware, we decrease the overall system weight, volume, cost, and complexity, and enhance the functional capabilities of soft systems. We start with describing the concept of SIMM and show how bistable shells are used as dynamic snap

hinges to fold and unfold the system into different patterns. Upon investigating the morphing cycle of the system, we theoretically identify the shell parameters that determine the snap-folding angle and snap-transition pressure and verify them with experimental and computational results. Then we demonstrate that assembling different snap modules into various modular origami and kirigami shapes can create multimorphing designs with versatile, adaptive properties such as multiterrain locomotion and unconventional object grasping.

RESULTS

Reversible multimorphing SIMM

A single snap unit is constructed by attaching a pneumatic cell, shaped as a cuboid, to a bistable elastomeric shell of a spherical cap shape surrounded by a flat rim; i.e., the shell snaps through upon positive pressure (inflation) and snaps back upon negative pressure (deflation) as shown in Figures 1A and 1B (see also Figure S1 in the supplemental material for additional details). To designate the two equilibrium modes of bistable states, we employ a binary code, denoting the initial pre-snap collapsed mode as s^0 and the post-snap popped-up mode as s^1. The overall SIMM is an assembly of interconnected snap units. Each unit is linked by a flat, flexible hinge to guide the folding pathway of the structure. To ensure spontaneous unfolding during snapback, a thin tendon connects the snap units. The length of the tendon is precisely determined to maintain its original length
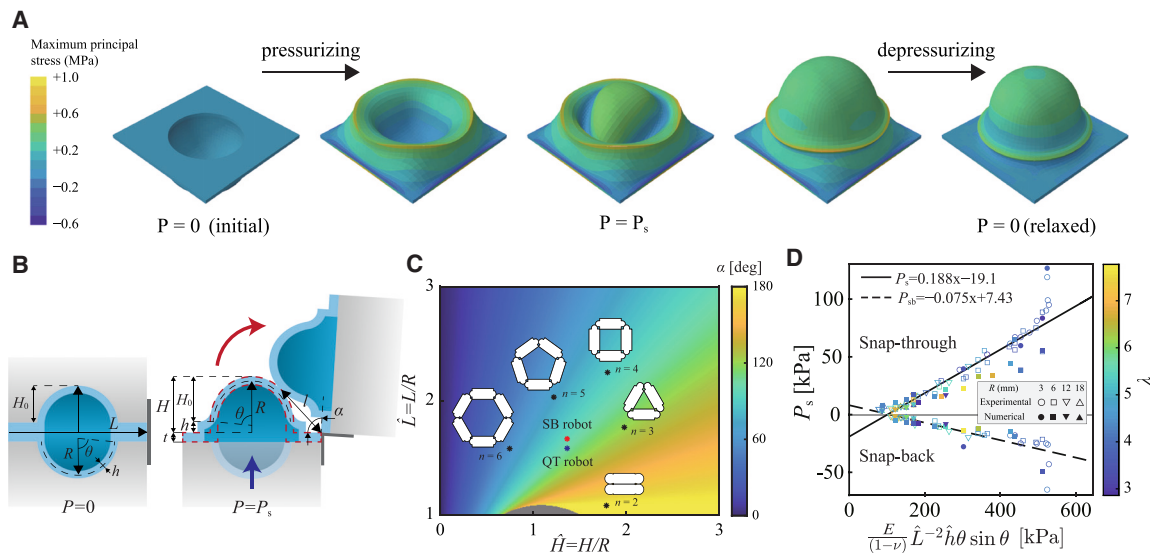
Figure 2. Mechanical characterization of SIMM

(A) Computational results of snap-through sequence of a spherical cap shell clamped at the edge of the square-shaped rim support, obtained by finite element analysis.

(B) Schematic illustration of folding of a SIMM upon snap-through of shells. Two adjacent snapped shells form a snap-folding angle α by tangential contact. The red dashed lines represent the simplified analytical profile of the post-snapped shell.

(C) Dependence of α on the normalized rim-clamped length $\hat{L}$ and overall height of post-snapped shell $\hat{H}$ predicted by our theoretical model. $\hat{h}$ is fixed as 1/6. The gray region represents physically impossible space. The data points for polygonal SIMM with n snap units, the spinning ball (SB) robot, and the quad-tessellation (QT) robot are indicated in the plot.

(D) Snap and snap-back pressure plotted against the analytically predicted parameter, $E\hat{L}^{-2}\hat{h}\theta \sin \theta/(1 - \nu)$. We use the rim clamp conditions with $\hat{L} = 3/2$ and $t = 1$ mm, and Poisson's ratio ν is assumed to be 0.5. Solid and dashed lines correspond to the lines of best fit for snap and snap-back pressures, respectively. Symbol color indicates the values of $\lambda = 12(1 - \nu^2)^{1/4}(\sqrt{R/h})\theta$.

(zero-stress state) in both modes, while undergoing momentary stretching just after the shells snap-back, which provides tension force pulling the units back together. In such a manner, the shells on the snap units work as dynamic snap hinges, pushing and pulling the neighboring cells and, as a result, folding the system into different patterns (see methods, fabrication of SIMMs, for details).

We now define the morphing cycle of a basic SIMM comprising two identical snap units (Figure 1C). We start from the initial pre-snap mode s^0, corresponding to the negative (inward) curvature of interconnected shells, and gradually increase the activation pressure P following path 1. Here, the pressure refers to the value relative to the atmospheric pressure. Once P exceeds the critical shell snap pressure $P_s(P \geq P_s)$, the shells snap through and pop out to attain the positive curvature, path 2. Then the two adjacent shells push each other, corresponding to the post-snap mode s^1, where the snap-folding angle defined as the angle between the two neighboring snap units as shown in Figure 1A is α. In path 3, the pressure in the snap units is reduced to the critical pressure for snap-back P_{sb}. Then the shells snap back to their initial states. Consequently, the tendon pulls the units back together, and the structure unfolds to the straight configuration of initial pre-snap mode s^0, path 4. This hysteretic behavior creates a unique path-dependent morphing cycle of SIMM.

It is unnecessary to constantly supply pressure to maintain each mode thanks to the bistable shells. We also note that monostable snap-through structures that allow for spontaneous

recovery upon removal of stimuli can be used if necessary. We can determine such structural stability of shells by tuning the geometric parameters (Figure S2C).

The nonlinear, stepwise response of snap-through can be integrated with various other continuous pneumatic actuators, such as a bellows-shaped pneu-net as shown in Figure 1D. Since our SIMMs store energy in bistable shells without deformation until a threshold strength of stimulus is reached, we can decouple the activation of the pneumatic actuator units from snap transformation of cap shells with only one input pressure. For instance, within the pressure range $P_{sb} < P < P_s$, we can extend or contract the bellows-shaped pneu-net without triggering the transformation between modes s^0 and s^1. The bellows actuators can be extended or contracted in either the straight (within path 1) or the folded (within path 3) configuration, allowing for multiple functions with a single pressure input.

Analysis of shape-shifting properties of SIMM

Although starting from the same planar form, origami and kirigami patterns can significantly differ in their final shapes depending on the folding order and the magnitude of folding angle. Therefore, to fully harness the shape-morphing potential of origami and kirigami patterns, precise individual control of different creases and cuts is crucial, which correspond to snap hinges in our SIMMs. To this end, we employ shells of varying geometries, whose snap-through properties are predicted through our analytical model (Figures 2A and S2). In the following, we

analyze the snapped profile and the critical snap pressure of the shells as functions of the geometric parameters defined in Figure 2B: mid-plane radius R, shell thickness h, opening angle θ, rim thickness t, and half cuboid width L.

The snap-folding angle α is defined as the angle formed by the two adjacent snapped shells that are in tangential contact with each other. Exterior geometry of post-snapped shell (Figure S3) gives the snap-folding angle as

$$\alpha = 2\tan^{-1}\left[\frac{\beta}{\sqrt{\widehat{L}^2+(\widehat{H}-\beta)^2-\beta^2}}\right]+2\tan^{-1}\left[\frac{1}{\widehat{L}}(\widehat{H}-\beta)\right],$$

(Equation 1)

where the non-dimensionalized parameters are such that $\widehat{L}=L/R$, $\widehat{H}=H/R$, $\widehat{h}=h/R$, and $\beta=1+\frac{1}{2}\widehat{h}$. In our model, the snap-folding angle α is assumed based on the geometric rigidity of the shells, which are thick enough to maintain a minimum thickness-to-radius ratio $(\widehat{h})$ to avoid substantial deformation under point forces such as the weight of neighboring cells. The specific threshold for this slenderness ratio, which ensures that the shells support the geometric assumptions without significant bending or indentation, is discussed in detail, along with the derivation of the geometric model, in Note S1, analysis of snap-folding angle. Our analytical model is consistent with experimentally and computationally measured α for various shells with $1<\widehat{H}<3$ and $0.1<\widehat{h}<0.5$ (Figures S3B and S3C). The color map in Figure 2C constructed by our analytical model illustrates the dependency of the snap-folding angle α on such factors as $\widehat{H}$ and $\widehat{L}$, enabling a design strategy for selecting appropriate shell geometries for target structures. Data points corresponding to various polygonal SIMMs with n snap units are presented in the figure.

To control the folding order of origami and kirigami, it is necessary to precisely engineer the snap and snap-back pressure of different shells, P_s and P_{sb}. We analyze the energies associated with the shell deformation to predict the snap pressure P of shells with rim-clamped boundary conditions. For the shells used in our experiments, we find that edge deformation governs the overall shell deformation. The strain energy potential of the shell region, W_{edge}, induced by (additive) natural curvature κ, can be scaled as:[43]

$$W_{edge}\sim\frac{Eh}{(1-\nu)}h^4\kappa^2\left(\frac{R}{h}\right)^{\frac{3}{2}}\sin\theta,$$

(Equation 2)

where E and ν are Young's modulus and Poisson's ratio, respectively. The potential energy induced by uniform pressure, denoted as $\Pi_P=P\int_W\Psi_3 dw$, can be scaled as $\Pi_P\sim Ph^2\kappa L^2$.[44] By scaling the two energies, $W_{edge}\sim\Pi_P$, we establish a pressure-curvature analogy similar to that of a complete sphere,[45]

$$\kappa\sim\frac{(1-\nu)}{E}R^{-\frac{3}{2}}h^{-\frac{3}{2}}L^2\frac{1}{\sin\theta}P.$$

(Equation 3)

This implies that a pressure P exerted against the convex side of a spherical shell is analogous to a curvature stimulus κ.

Substituting the critical curvature stimulus at snapping, $\kappa_s\sim\theta/\sqrt{Rh}$,[43] in Equation 3, we finally scale the snap-through pressure of rim-clamped shells as a function of E, $\widehat{L}$, $\widehat{h}$, and θ:

$$P_s\sim\frac{E}{(1-\nu)}\widehat{L}^{-2}\widehat{h}\theta\sin\theta.$$

(Equation 4)

Figure 2D demonstrates that our scaling aligns well with both experimental and computational results for the snap-through pressure across shells with varying values of $\lambda=[12(1-\nu^2)]^{1/4}(\sqrt{R/h})\theta$. This parameter, which scales the ratio between the stretching and bending energy densities $(\sim(\mathcal{E}_s/\mathcal{E}_b)^{1/4})$, is often used for determining various shell behaviors, such as the stability of spherical shells, as illustrated in Fig. S2C.[46] The snap-back pressure P_{sb} also conforms to our scaling, reflecting similarities in the snapping mechanism, although it is influenced by residual stress.

In our model, we adopt a theoretical framework that assumes idealized axisymmetric deformations of perfect shells, focusing primarily on edge bending while neglecting any prior local buckling effects. However, shells with imperfections may exhibit significant local buckling, requiring an alternative approach to predict snap-through pressures accurately. One way to deal with these situations is by deliberately introducing controlled imperfections, such as localized dimple-like defects, to modulate the buckling behavior.[47,48] Precisely engineered imperfections could significantly reduce the imperfection sensitivity to defects, and allow the system to achieve desired snap-through pressures with accuracy. This work concentrates on the established model for P_s in order to demonstrate capabilities of multimorphing SIMM mechanisms, with further details on managing imperfections reserved for future research. Further discussion on the derivation of P_s, as well as the diverging trend observed beyond the specified pressure ranges in Figure 2D and the effect of imperfections, can be found in Note S2: supporting theory for snap-through pressure.

Principles of path-dependent morphing transition

After demonstrating the controllability of snap-folding angle and snap pressure using shells with varying geometry, we now construct a multimorphing structure whose deformation can be controlled by a single pressure input. Each state of the n-shell system can be expressed as $s^{a_1 a_2 \cdots a_i \cdots a_{n-1} a_n}$, where $a_i\in\{0,1\}$ indicates the bistable state of the ith shell. The index i is arranged according to the sequence of snap pressures, placing shells with higher snap pressures at the sequence's end. The snap-folding angle, snap-through pressure, and snap-back pressure of the ith shell are denoted as α_i, $P_{s,i}$, and $P_{sb,i}$, respectively.

Figure 3A demonstrates an example of morphing transition of SIMM consisting of three snap units having two interconnecting shell pairs with different snap criteria, termed "thin" and "thick" for low and high snap-through pressure. Starting from the straight configuration s^{00}, during the inflation stage (solid lines), the thin shell pair snaps first, as pressure is increased to $P=P_{s,1}$, forming an inverted L shape s^{10}. Then at higher pressure $P=P_{s,2}$, the thick shell pair snaps, forming an inverted-C shape s^{11}. During the deflation stage (dashed lines), the thin shell pair snaps back first at $P=P_{sb,1}$, forming a rotated-L shape s^{01},
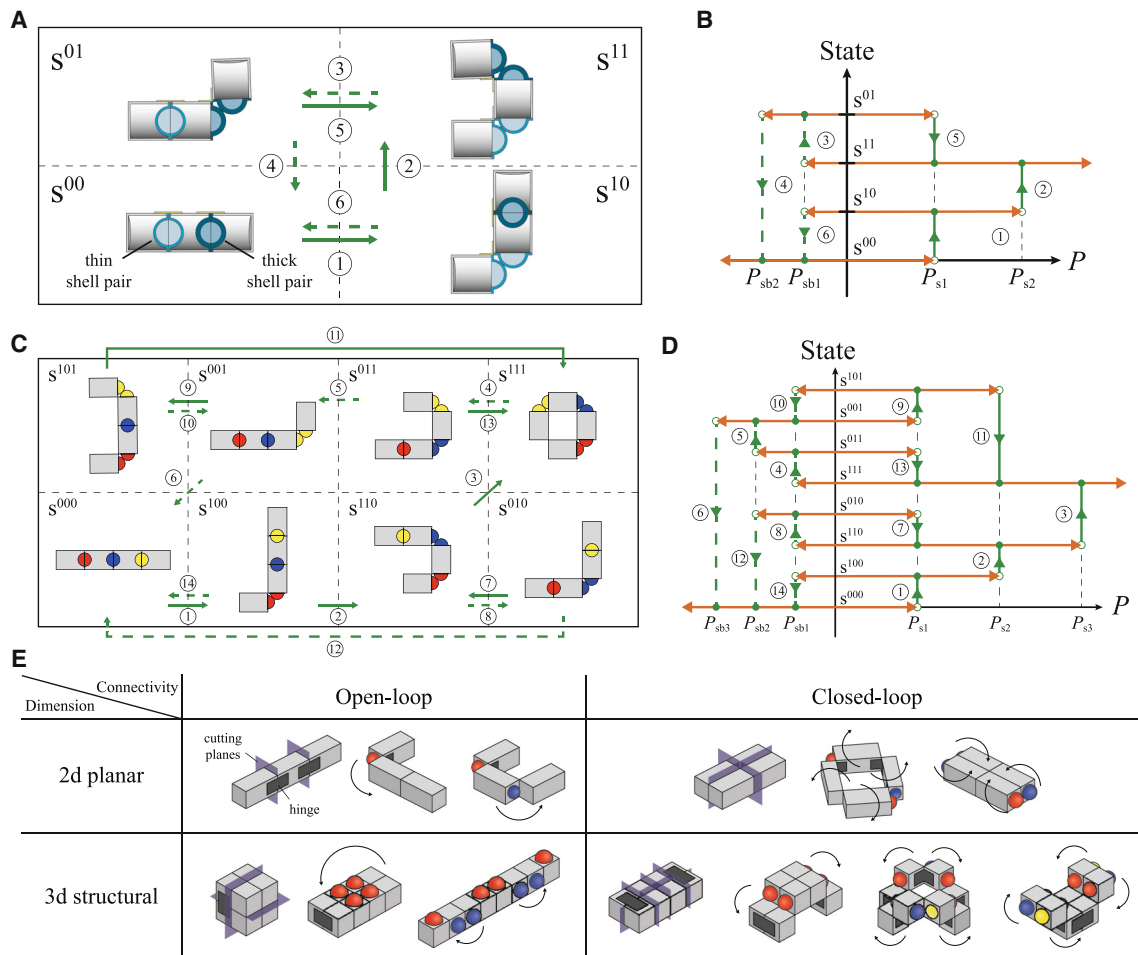
Figure 3. Morphing transition patterns of SIMMs

(A and B) Schematic illustration (A) and (B) corresponding pressure-state diagram for the path-dependent transition cycle of a SIMM system consisting of three aligned snap units.

(C and D) Schematic illustration (C) and (D) corresponding pressure-state diagram for the path-dependent transition cycle of a SIMM system with four aligned snap units. Green solid and dashed lines correspond to snap-folding and snap-back unfolding procedures, respectively. Orange lines represent the possible pathways of continuous pneumatic actuations in each state.

(E) Classification of morphing transition patterns in SIMM, utilizing basic cuboidal snap units.

and then the thick shell pair snaps back at lower negative pressure $P = P_{sb,2}$, restoring the structure to its initial state s^{00}. Note that the thin shell pair always snaps and snaps back prior to the corresponding action of the thick shell pair, and thus the intermediate states have different shapes during the inflation (inverted-L) and deflation (rotated-L) stages. In other words, we can achieve all possible configurations otherwise unachievable through anhysteretic morphing mechanisms, with combinations of activated (1) and deactivated shells (0) through precise sequencing of pressure inputs (Figure 3B). This allows the system to leverage maximum of 2^n number of configurations instead of just $2n$, for n number of different types of shell pairs used.

To transition from the initial all-zero state $s^{0\cdots0}$ to an arbitrary desired state $s^{a_1a_2\cdots a_i\cdots a_{n-1}a_n}$, where a_i $(i = 1, \cdots, n)$ can be either 0 (pre-snap) or 1 (post-snap), the protocol for the input pressure cycle is as follows: first, identify the largest index k for which

$a_k = 1$, indicating the shell pair that snaps last. The snap-through pressure criteria for the kth shell is $P_{s,k}$. Subsequently, find the largest index $l < k$ where $a_l = 0$, establishing the snap-back pressure, $P_{sb,l}$, for the lth shell. This iterative process of alternating between 1s and 0s progresses until the first shell (a_1). To achieve the desired state, the pressure is sequentially adjusted: first increased to $P_{s,k}$ to activate the snap-through of the targeted shell pair(s), then decreased to $P_{sb,l}$ for snap-back, and so forth, following the established sequence until all specified states are reached. For example, in the case of a triple-shell SIMM, to transition from the state s^{000} to s^{101}, the pressure is first increased to $P_{s,3}$, activating the snap-through for all three types of shell pairs. It is then decreased to $P_{sb,2}$, causing the first two shell pairs to snap back and, finally, the pressure is increased once more to $P_{s,1}$, to re-activate the snap-through of the first shell pair as shown in Figures 3C and 3D.

Combined with the design principle of snap-folding angles, this approach leads to a wide array of modular origami and kirigami shapes distinguished by their connectivity and the dimension of configuration space, as illustrated in Figure 3E and Figure S6. We see that our adaptable, transformable structures can realize modular kirigami architectures. It is worth noting that the adaptability of our approach is not limited to variations in snap-folding angles and pressures; snap units of varied geometries, such as tetrahedrons (Figure S7), can be employed to achieve desired modular origami and kirigami shape morphing. Incorporating concepts such as rotational joints and rigid bar-linkages, as explored in modular architected materials,[27] and extending these to include deformable bar-linkages to represent continuous pneumatic actuators could further enhance the systematic assembly and versatility of these structures. Furthermore, these snap units can be pneumatically actuated to function in any configuration, allowing us to showcase examples of multifunctional soft robots in the following.

Multiterrain locomotive soft robot

We now present a soft robot constructed on the basis of SIMM that can adaptively metamorphose into multiple forms for multiterrain locomotion including crawling and cable climbing. Although several soft climbing robots have been demonstrated previously,[9,49,50] their locomotions have been limited on a single terrain. Inspired by the spinning ball origami (also known as *Twirligig*, see also Figure S10A), here we develop a crawling soft robot capable of conformable locomotion on two distinct terrains, a flat surface and a curved cable, using a single input pressure control for both transformation and locomotion (Figure 4; Video S1).

We build a single snap unit of an elastomer cuboid with an interior gas chamber having two bistable cap shells at the two opposite faces as shown in Figure 4A. By attaching the snap units to both ends of a bellows-shaped extension actuator, we construct a single-extension snap module (Figure 4B). Next, we align three extension-snap modules side by side and connect the neighboring snap units via flexible hinges and tendons, replicating the configuration of a three-strip *Twirligig* (Figure 4C). This corresponds to a soft pneumatic robot capable of shifting shapes between flat (mode s^0) and cylindrical (mode s^1), and of elongating and recovering in both the flat and cylindrical modes. We affixed ratchet legs to both upper and bottom surfaces of each snap unit for the robot to selectively hook and release the terrain (ground or cable) depending on the body posture for directional propulsion (Video S2).

Initially, our robot can crawl like an earthworm on flat surfaces (mode s^0). The robot wriggles forward by periodically extending and returning to its initial length as the actuation pressure oscillates between 0 and $P = 13$ kPa ($< P_s = 13.5$ kPa) (Figure 4D). Although three pressure tubes are depicted in the figure, it is important to note that these tubes are interconnected, converging into a single channel at the end of the setup, which simplifies the control system by reducing the number of independent pressure sources required for operation. When the robot reaches a cable, it curls up into a 3D cylindrical shape (mode s^1), grasping and enclosing the cable by snapping all the shells at pressure $P = P_s = 13.5$ kPa (Figure 4E). The transition to

mode s^1 occurs in less than 0.1 s, utilizing the inherently fast nature of snap-through dynamics, which contrasts sharply with the slower cyclic locomotion of the robot. The cyclic locomotion is constrained primarily by the frequency of the pneumatic controllers (1/4 Hz in our demonstrations) and the influx of air. Once transformed, the robot extends and recovers periodically, now in a cylindrical shape, to propel itself on the cable ($0 \leq P \leq 13$ kPa). The flexible structure, realized by both the consisting soft materials and the gaps in between the extension actuators, resembling kirigami cuts of a *Twirligig*, enables the robot to smoothly bend while climbing the curved section of the cable (Figure 4F). When the pressure is decreased to $P = P_{sb} = -5$ kPa, all the shells snap back, and the robot reconfigures into its flat mode s^0, losing its grip of the cable and landing on the ground (Figure 4G). Simultaneous folding or unfolding of all the snap hinges enhances the robot's capability to transition seamlessly between different terrains. Furthermore, the robot's highly compliant structure allows it to adeptly navigate through narrow curved tunnels 3.2 mm wide—only 1.16 times the height of the robot—with curvature 0.08 mm^{-1}. This capability is demonstrated as the robot smoothly transitions from the tunnel to climbing vertically along a cable (Figure 4H). The robot can bend up to 180° without damage, constrained only when the front and rear cells make contact. It is also worth noting that during the transition from the tunnel to the cable, the front cells initially wrap around the cable while the rear cells are still inside the tunnel. The structural conformability demonstrated here further highlights the potential of our SIMM robots as multifunctional, adaptable systems for various scenarios and environments (Video S3).

Bidirectional locomotive and deployable soft robot

Here, we present a reversibly deployable soft robot that employs planar kirigami tessellation combined with modular origami and transforms by pneumatically controlled snapping at cutting patterns. To demonstrate the adaptability of our design to various deployable structures, we selected quad-tessellation (QT), also known as *rotating rectangles*. This 2D kirigami pattern, formed by making partial cuts in flat sheets, enables compact forms to expand into more open structures. We build a single bending-snap module by attaching a bistable cap shell at one end of pleated-cuboidal bending actuator as shown in Figure 5A. The two-by-two array of these bending-snap modules, connected via flexible hinges and tendons between the cap shells, yields a transformable robot, as shown in Figure 5B. The QT robot can assume three different shapes according to the opening and closing of the edges: the *x*-directionally aligned closed shape, the deployed shape with an empty square hole, and the *y*-directionally aligned closed shape.

We employ two types of shells having distinct sets of snap-through and snap-back pressure (type 1: $[P_{s,1}, P_{sb,1}] = [18, -7]$ kPa, type 2: $[P_{s,2}, P_{sb,2}] = [24, -12]$ kPa), which allows us to reach the *x*- or *y*-directionally aligned closed shapes in a controlled manner. Starting from *x*-directionally aligned closed configuration corresponding to mode s^{00} with all the cap shells snapped back ($P < P_{s,1}$), increasing the interior pressure ($P_{s,1} \leq P < P_{s,2}$) snaps the type 1 shells (mode s^{10}), which opens the robot to unveil the square hole. Further increase of the
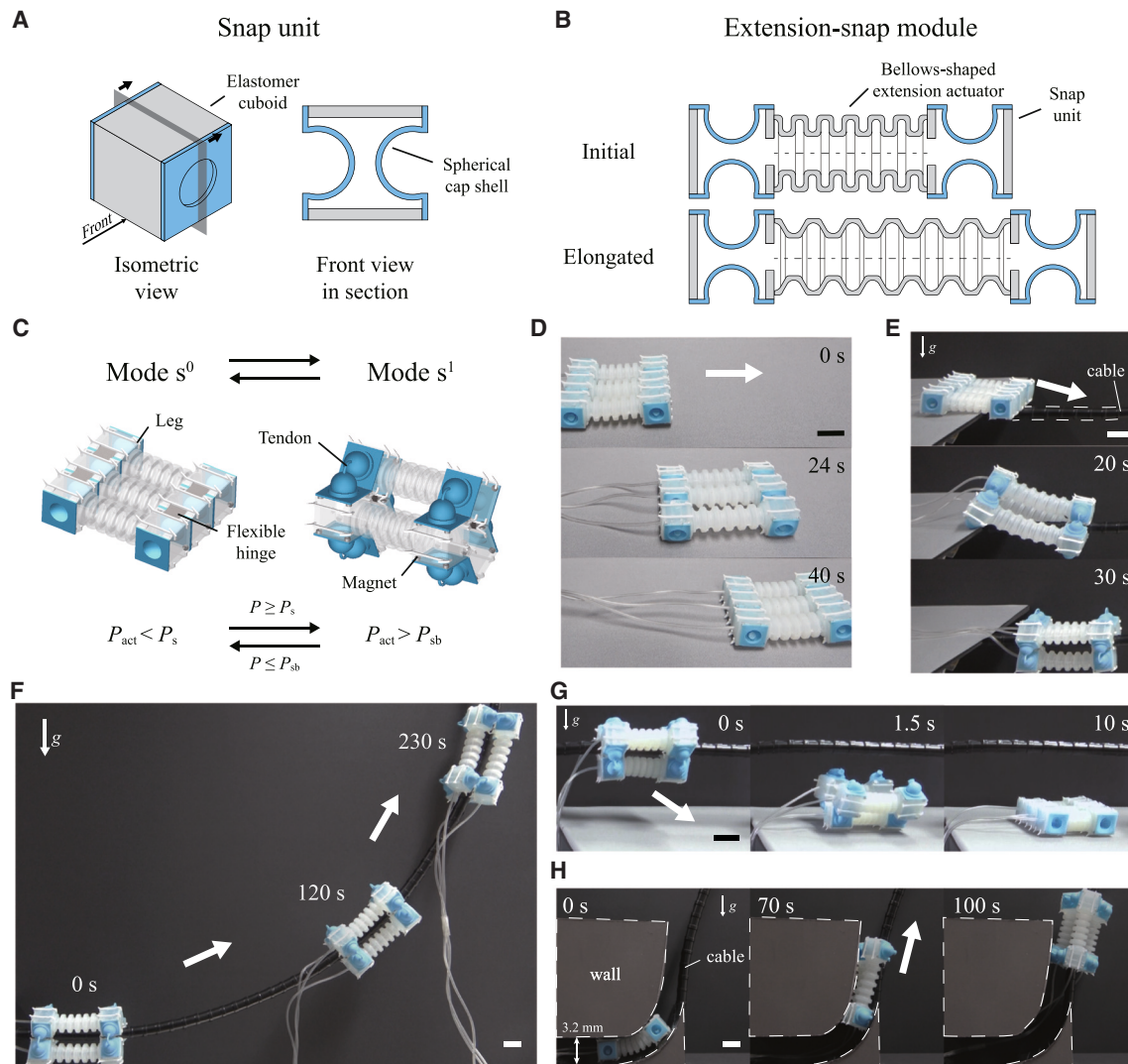
Figure 4. Multiterrain locomotive soft robot

(A) Schematic of the snap unit and (B) the extension-snap module.

(C–H) Schematic of the SIMM spinning ball robot (C). The robot transforms from ground crawling mode s^0 to cable climbing mode s^1. The robot can (D) crawl on a flat surface, (E) relocate from ground to a cable by instantaneous snap-through, (F) compliantly climb the cable, (G) relocate back from the cable to ground by snap-back, and (H) maneuver from a narrow tunnel to a vertical cable. Scale bars, 20 mm.

pressure ($P \geq P_{s,2}$) snaps the type 2 shells (mode s^{11}), which closes the robot but at a configuration 90° rotated counter-clockwise. For cyclic bending, the interior pressure oscillates periodically between 0 and 17 kPa, staying below the snap-through threshold of type 1 shells ($P < P_{s,1} = 18$ kPa) to maintain bending without initiating snap transitions. Reducing the pressure below $P_{sb,1}$ causes the robot to open again due to snap-back of the type 1 shells (mode s^{01}). Although the two different modes, s^{10} (thin shell snapped) and s^{01} (thick shell snapped), have distinct shell configurations, they result in identical deployed shapes in terms of modular origami and kirigami pattern, reducing the unique configurations of the robot to $2^2 - 1 = 3$. Further decrease of the pressure ($P \leq P_{sb,2}$) closes the robot with snap-back of the type 2 shells (mode s^{00}). The resulting configuration is identical to the original x-directionally aligned QT.

We demonstrate a potential application of the QT robot by attaching ratchet legs on the bottom of bending-snap modules (Video S4). The pleats on the top and sides of the cuboid, with the assistance of a stiffer layer on the bottom, allow the actuating unit to bend over with the positive interior pressure and return to the straight configuration at zero or negative pressure. Thus, periodic oscillations of the pressure input between 0 and $P_{s,1}$, as shown in Figure 5C ($0 < t < 160$ s), enables the aligned QT robot to propel itself like an inchworm as shown in Figure 5D. A net attached to the bottom of the QT robot is deployed when s^{10} is reached by increasing the pressure over $P_{s,1}$ ($t = 160$ s in Figure 5C), which can be used to store and carry a target as shown
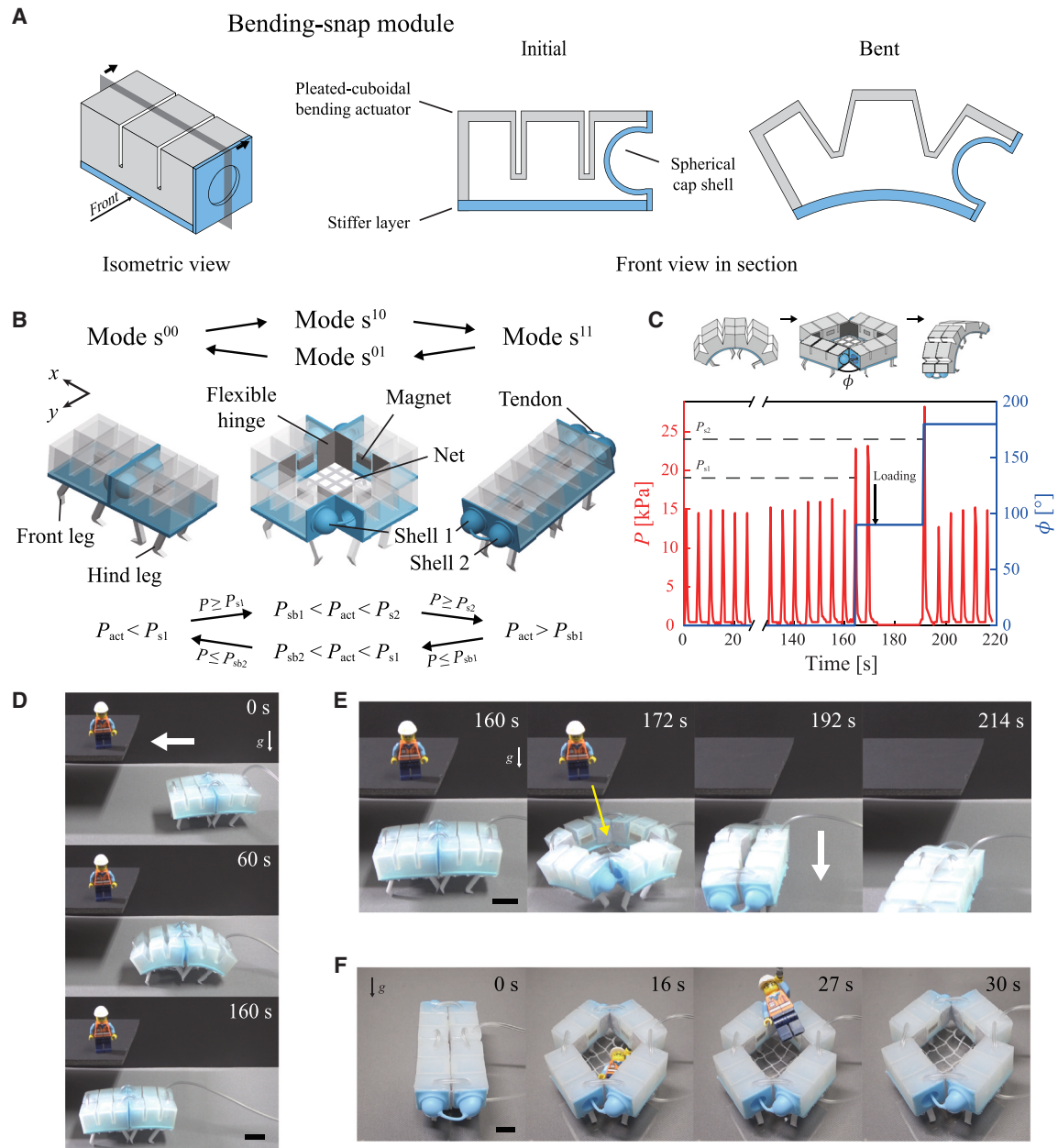
Figure 5. Shape-shifting and deployable soft robot

(A) Schematic of the bending-snap module.

(B) Schematic of the SIMM QT robot. Utilization of two types of shells with different snap thresholds enables the transition from x-directionally aligned closed mode s^{00} to kirigami deployed mode s^{10} or s^{01} to y-directionally aligned closed mode s^{11}.

(C–E) Experimentally measured time-pressure curve and corresponding snap-folding angle ϕ (C) corresponding to the robot locomotion and cargo (or the rescued) transportation in (D and E). The robot first (D) crawls in the x-direction to approach the target position and then (E) snaps open to deploy the cargo net. Once the target is safely placed on the net, the robot transforms to mode s^{11} and crawls in the y-direction.

(F) The robot snaps back into mode s^{01} to release the target. Scale bars, 20 mm.

in Figure 5E (t = 172 s). The robot is closed in a direction perpendicular to the original by the increase of pressure over $P_{s,2}$ (t = 192 s in Figure 5C), and then crawls in a path perpendicular to the original via periodic oscillations of the pressure (192 s < t < 214 s in Figure 5C), as shown in Figure 5E. The ratchet legs are

configured so that the robot can move in its aligned direction even after QT rotation (Figure S13; Video S5). The cargo net, attached only to the four outer edges, can expand to an interior volume of up to 45 cm^3, which is 84% of robot's body volume. Therefore, it can store cargo undamaged, thanks to its

hammock-like drooping when closed. Finally, the cargo net is opened by changing to mode s^{01} as the pressure is reduced below $P_{sb,1}$, allowing the target to be taken out, as shown in Figure 5F.

DISCUSSION

Our study highlights the potential of a soft and foldable structure with snapping internal connections, presenting a simple yet effective approach to achieving multifunctionality in pneumatic actuators. Our mechanical model of shell snapping, based on the geometric relationships and energy minimization allows us to predict both shell snap pressure and the resulting snap-folding angle, which are scalable in magnitude and size. To this date, the actuation of soft robots utilizing elastic structural instabilities mainly addressed rapid motion and high energy release during snap-through buckling.[34,37,51] Our work broadens the scope by emphasizing on utilizing snapping structures as a control mechanism for controllable shape transformations.

By combing n types of shells with different critical transition stimuli, the SIMM system can attain up to a maximum of 2^n different configurations, making the system highly programmable. Each state can be achieved by precisely ordered control of pressure that motivates selective snapping at designated locations. We have introduced a simple classification system for transformable shapes based on cell connectivity and dimension, yet future work is called for to fully exploit the vast array of potential designs.

Leveraging the novel concept of snap inflatable modular metastructures, our research introduces reconfigurable soft robots for multifunctional applications, controlled by a single pressure input. We present two designs that exemplify the ingenuity of SIMM: the spinning ball and QT robots. The spinning ball robot, inspired by *Twirligig*, showcases adaptability across various terrains through its ability to transition between flat and cylindrical modes. The QT robot, drawing from the *rotating rectangles*, is capable of crawling, payload transport, and turning directions, achieved by incorporating shells with two distinct snap pressures.

The design strategy proposed in this work is a promising solution for the multifunctional capability of soft robots by harnessing the multistability of curved elastic shells and reconfigurable modular origami and kirigami structures. The ability to trigger the instability of each snap unit with a single input significantly simplifies the system without compromising potential combinational reconfigurability.[52] Furthermore, the SIMM is composed of widely used silicone elastomer and thus can be effectively integrated with existing elastomer-based soft systems.

Soft pneumatic actuators can be scaled from micro to macroscales, with applications extending to extremely large robots.[53] Similarly, our snap-through folding principle with modular assemblies offers significant scalability potential while posing several challenges. For instance, scaling to applications involving heavy payloads, such as an actual person instead of the demonstrated figurine, will require further research to enhance material strength and optimize pneumatic control mechanisms. Key considerations for scaling include the deformation principle's applicability across length scales, material se-

lection, manufacturing complexity, and actuation time. Non-dimensionalization of spherical shell parameters (R, h, L, H, t) confirms that critical pressure and folding angles remain consistent across scales. However, structural rigidity, as detailed in Note S1, scales differently and may decrease with reductions in radius and thickness, making the snapped hinge more susceptible to indentation from external forces.

In this work, we solve the snap-through behavior using linear elasticity within the continuum mechanics framework. This approach, assuming a constant modulus, is suitable as the strains in the system range mostly remain within the linear elastic regime despite geometric nonlinearity. However, localized regions, such as the rim boundary, may experience higher strains (∼0.5), potentially exceeding the linear range. While insignificant for this study, extreme geometries or unconventional shell structures may require advanced models (e.g., hyperelasticity) or dynamic analyses to account for strain-rate effects. Material selection poses challenges due to these localized strains, but the majority of the structure experiences significantly lower strains (typically below 0.05), mitigating fatigue concerns and allowing the use of a broader range of materials. Future work could explore alternative structures such as conical shells,[54] which exhibit lower strain distributions, or bistable origami units,[23] which may enhance robustness across scales. Scaling pneumatic or hydraulic actuation introduces additional challenges, particularly the time required for flow transfer. Larger actuation volumes and channel lengths amplify viscous effects, slowing pressurization and depressurization, while miniaturization may encounter similar issues due to reduced channel widths. The rapid movement of snapping structures partially mitigates these limitations,[30] but the time to reach the critical snapping point remains a challenge warranting further study.

Extending our design to complex machines presents unique constraints. For example, the spatial volume occupied by snapped shells must remain unobstructed until snap-back occurs, limiting certain configurations. Connections between cells must ensure kinematic compatibility to allow deformations such as extension or bending without interference. Systematic strategies, such as leveraging computational tools for inverse design, creating libraries of morphing configurations, or exploring alternative polyhedral geometries, could address these challenges and unlock new possibilities for modular assemblies tailored to specific applications. Incorporating deformable bar-linkages into the modular design could further expand the range of achievable configurations, combining discrete snap-through transitions with continuous actuation functions for enhanced reconfigurability.

On the other hand, while our SIMM mechanism significantly reduces the reliance on auxiliary components, a minimal number of external control components remain essential for managing precise pressurization sequences. Moving forward, integrated control strategies such as fluidic logic could further simplify the actuation process,[9,18,55] potentially eliminating the need for external valves and regulators. Future studies could concentrate on utilizing recent developments in electronics-free pneumatic circuits[36] to achieve untethered actuation of SIMM. Such development could greatly enhance the utility of our system in scenarios where minimizing space and weight is essential. Upon

combination with a myriad of foldable structures, our study lays the groundwork for diverse applications of morphing systems with deployability, scalability, and controllability in such fields of minimally invasive surgery and search and rescue operations.

METHODS

Fabrication of SIMMs

A basic snap unit is composed of a pneumatic cell having an elastomeric spherical cap shell surrounded by a flat rim. A single SIMM is constructed by connecting the two snap units with a flexible hinge and a tendon. The shells (1:1 ratio mixture of Smooth-Sil 950/Dragon Skin 30, Smooth-On) and pneumatic cells (1:1 ratio mixture of Dragon Skin 30/Dragon Skin 10, Smooth-On) are made of silicone-based elastomers by injecting uncured elastomers in 3D-printed molds and curing for 1 h in the oven at 50°C. Flat, flexible hinges are laser-cut from a piece of fabric (polyester 100%, 0.2 mm thickness) into rectangular shapes. Pieces of the tendon are fabricated by injecting uncured elastomers (1:1 ratio mixture of Smooth-Sil 950/Dragon Skin 30, Smooth-On) into a tygon tube with an inner diameter 0.8 mm (E-3603, Saint-Gobain) as a mold and curing for 1 h in the oven at 50°C. After fully curing a long strip of tendon, it is pulled out of the tube to be cut into different lengths for use. These components are bonded by applying uncured elastomer (Dragon Skin 30, Smooth-On) on the interfaces and curing for 1 h in the oven at 50°C.

Measurement of snap properties

Measurement of the snap-through and snap-back pressures, along with the corresponding snap-folding angle, is performed by clamping the edges of the square-shaped rim support of shells between two 3-mm-thick acrylic panels. The clamped shells and the acrylic panels are bolted onto an empty 3D printed chamber with a tube connected to a nitrogen tank for gas supply as a pressure source. Pressure values at the moment of snap-through P_s of various shells are monitored using a digital pressure gauge (Autonics, PSAN-C01CV). The snapped shells are clamped in a reversed fashion to measure the snap-back pressure P_{sb} in the same procedure (Figure S2).

Young's moduli of elastomers are measured using ASTM D 412 series dog-bone specimens under uniaxial loading by an Instron 34SC-1 mechanical testing machine with a 500-N load cell at a loading rate of 100 mm/min. The measured values are given in Table S1.

Computational analysis of snap properties

The FEM (finite element method) simulation is performed using a commercial package, ABAQUS/STANDARD. Consistent with the experiments, the structures are modeled as incompressible hyperelastic material, neo-Hookean solids, with reduced hybrid 3D elements, C3D8RH with minimized distortions. The shells are discretized with regular mesh with 72 and 5 elements in the azimuthal and thickness directions. For the meridional direction, equivalent mesh sizes are located depending on the opening angle θ (between 12 and 30 elements). The plates are discretized with regular mesh with 36 and 5 elements in the planar and thickness directions, respec-

tively. All analyses are based on the nonlinear geometric basis and convergence test.

The simulations are implemented with three steps: snap, relaxation, and snap-back motions. Comparing the three analyses (1) static Riks (arc length method), (2) static with energy dissipations, and (3) quasi-static dynamics, we verify the results, validating with experimental data.

(1) Snap motion: first, the shells are loaded by uniform pressure, $P_{cr} = 2E/[3(1 - \nu^2)]^{1/2}(h/R)^2$ to find the snap pressure, P_s. Static Riks, static with energy dissipations, and quasi-static dynamics methods are used.

(2) Relaxation: the uniform pressure is removed to find the snapped shell geometries. Static with energy dissipations and quasi-static dynamics methods are used.

(3) Snap-back motion: last, the snapped shells are loaded by uniform pressure, $-P_{cr}$ describing the depressurization and snap-back motion to find the snap-back pressure, P_{sb}. Static Riks, static with energy dissipations, and quasi-static dynamics methods are used.

Fabrication of spinning ball robot

We fabricate cubic snap units (1:1 ratio mixture of Dragon Skin 30/Dragon Skin 10, Smooth-On) with snapping shells ($R = 6$ mm, $h = 1$ mm, $\theta = 105°$) on two opposite sides using the method prescribed above. A total of eight cylindrical magnets of diameter 3 mm and thickness 1 mm are inserted inside the corners of contacting faces, one in each corner, to assist the adhesive forces of the folded units. Flat, circular magnets are attached to the bottom of the snap units to assist the stabilization of the cylindrical mode. One lateral side of each unit is punched with a ventilation hole to allow airflow through the extension actuator.

An extension actuator made of elastomer is fabricated by adhering two identical half-bellows together, each molded using two-part 3D printed molds. The bellows design was selected over other directional extension and contraction mechanisms, such as the McKibben actuators[56] or fiber-reinforced actuators,[57] due to its simple fabrication process, which eliminates the need for additional components. After comparing three different designs, we selected a bellows actuator made of Dragon Skin 10 (Smooth-On), with an initial length of 20 mm and a wall thickness of $t = 1$ mm. This design achieved a sufficiently large elongation (1.97 times its original length at 13.5 kPa) without significant ballooning, making it suitable for the intended application.

Then, two snap units are attached along the two ends of a single extension actuator to prepare a single extension-snap module. Acrylic ratchet legs fabricated by laser cutting are attached to both the top and bottom sides of snap units, two on each side, to ensure motion even when the robot lands upside down during transition between terrains. We then connect three snap-extension modules side-by-side with flat, flexible hinges made of fabric as above to create a SIMM spinning ball robot. Details of the design are presented in Fig. S8–S10.

Fabrication of QT robot

A cuboid-shaped pneumatic cell with a pleated top (1:1 ratio mixture of Dragon Skin 30/Dragon Skin 10, Smooth-On) is

attached to a stiffer bottom layer (1:1 ratio mixture of Smooth-Sil 950/Dragon Skin 30, Smooth-On) of 2 mm thickness to fabricate a bending actuator. This design, incorporating a corrugated top and a relatively stiff bottom, enables angular deformation of up to $36.3°$ at 17 kPa for a single bending-snap module. Then, a shell is attached on one side of the bending actuator to prepare a single bending-snap module.

Two types of shells with different thicknesses (R = 6 mm, h = 1 and 1.2 mm, θ = 105°) are used to discriminate their snap-transition thresholds. By cross-orienting four bending-snap modules diagonally in a 2×2 array so that the different types of shells make face-to-face contact, we create a SIMM QT robot. Flat, rectangular magnets are attached to the inner side walls of the snap units to assist the stabilization of the closed modes. The rescue net is bonded along the bottom inner edges of bending-snap modules so that it can fold and deploy together with the robot. Acrylic ratchet legs are attached to the bottom side of the modules to yield asymmetric friction coefficients. The legs are arranged so that the functional legs (front and rear) are always directionally oriented upon mode change. Details of the design are presented in Figures S11–S13.

RESOURCE AVAILABILITY

Lead contact

Requests for further information and resources should be directed to and will be fulfilled by the lead contact, Ho-Young Kim (hyk@snu.ac.kr).

Materials availability

This study did not generate new unique reagents.

Data and code availability

- All data reported in this paper will be shared by the lead contact upon request.
- This paper does not report original code.
- Any additional information required to reanalyze the data reported in this paper is available from the lead contact upon request.

AUTHOR CONTRIBUTIONS

J.-S.P., J.-Y.S., and H.-Y.K. proposed and designed the research. J.-S.P. conducted the theoretical analyses. K.K. and A.L. conducted the computational simulations. J.-S.P. designed and fabricated models. J.-S.P. performed the experiments. J.-S.P., A.L., and H.-Y.K. analyzed the results. J.-S.P., A.L., J.-Y.S., and H.-Y.K. wrote the paper.

DECLARATION OF INTERESTS

H.-Y.K. and J.-S.P. are the inventors on the patent applications (1: 18/540,757, USA; 2: 1020230005455, Republic of Korea; 3: 1020230005503, Republic of Korea) submitted by SNU R & DB Foundation that covers the soft robotic applications using SIMM mechanism.

SUPPLEMENTAL INFORMATION

Supplemental information can be found online at https://doi.org/10.1016/j.xcrp.2025.102448.

REFERENCES

1. Shepherd, R.F., Ilievski, F., Choi, W., Morin, S.A., Stokes, A.A., Mazzeo, A.D., Chen, X., Wang, M., and Whitesides, G.M. (2011). Multigate soft robot. Proc. Natl. Acad. Sci. USA *108*, 20400–20403.

2. Brown, E., Rodenberg, N., Amend, J., Mozeika, A., Steltz, E., Zakin, M.R., Lipson, H., and Jaeger, H.M. (2010). Universal robotic gripper based on the jamming of granular material. Proc. Natl. Acad. Sci. USA *107*, 18809–18814.

3. Martinez, R.V., Branch, J.L., Fish, C.R., Jin, L., Shepherd, R.F., Nunes, R.M.D., Suo, Z., and Whitesides, G.M. (2013). Robotic tentacles with three-dimensional mobility based on flexible elastomer. Adv. Mater. *25*, 205–212.

4. Yang, D., Mosadegh, B., Ainla, A., Lee, B., Khashai, F., Suo, Z., Bertoldi, K., and Whitesides, G.M. (2015). Buckling of elastomeric beams enables actuation of soft machines. Adv. Mater. *27*, 6323–6327.

5. In, H., Kang, B.B., Sin, M., and Cho, K.-J. (2015). Exo-Glove: A wearable robot for the hand with a soft tendon routing system. IEEE Robot. Autom. Mag. *22*, 97–105.

6. Deimel, R., and Brock, O. (2016). A novel type of compliant and underactuated robotic hand for dexterous grasping. Int. J. Robot. Res. *35*, 161–185.

7. Hawkes, E.W., Blumenschein, L.H., Greer, J.D., and Okamura, A.M. (2017). A soft robot that navigates its environment through growth. Sci. Robot. *2*, eaan3028.

8. Hu, W., Lum, G.Z., Mastrangeli, M., and Sitti, M. (2018). Small-scale soft-bodied robot with multimodal locomotion. Nature *554*, 81–85.

9. Lee, W.-K., Preston, D.J., Nemitz, M.P., Nagarkar, A., MacKeith, A.K., Gorissen, B., Vasios, N., Sanchez, V., Bertoldi, K., Mahadevan, L., and Whitesides, G.M. (2022). A buckling-sheet ring oscillator for electronics-free, multimodal locomotion. Sci. Robot. *7*, eabg5812.

10. Hwang, D., Barron, E.J., Haque, A.B.M.T., and Bartlett, M.D. (2022). Shape morphing mechanical metamaterials through reversible plasticity. Sci. Robot. *7*, eabg2171.

11. Ze, Q., Wu, S., Dai, J., Leanza, S., Ikeda, G., Yang, P.C., Iaccarino, G., and Zhao, R.R. (2022). Spinning-enabled wireless amphibious origami millirobot. Nat. Commun. *13*, 3118.

12. Park, C.J., Ha, J., Lee, H.-R., Park, K., Sun, J.-Y., and Kim, H.-Y. (2023). Plant cell-like tip-growing polymer precipitate with structurally embedded multistimuli sensing ability. Proc. Natl. Acad. Sci. USA *120*, e2211416120.

13. Buckner, T.L., Yuen, M.C., Kim, S.Y., and Kramer-Bottiglio, R. (2019). Enhanced variable stiffness and variable stretchability enabled by phase-changing particulate additives. Adv. Funct. Mater. *29*, 1903368.

14. Shah, D.S., Powers, J.P., Tilton, L.G., Kriegman, S., Bongard, J., and Kramer-Bottiglio, R. (2020). A soft robot that adapts to environments through shape change. Nat. Mach. Intell. *3*, 51–59.

15. Patel, D.K., Huang, X., Luo, Y., Mungekar, M., Jawed, M.K., Yao, L., and Majidi, C. (2023). Highly dynamic bistable soft actuator for reconfigurable multimodal soft robots. Adv. Mater. Technol. *8*, 2201259.

16. Rus, D., and Tolley, M.T. (2015). Design, fabrication and control of soft robots. Nature *521*, 467–475.

17. Kim, W., Byun, J., Kim, J.-K., Choi, W.-Y., Jakobsen, K., Jakobsen, J., Lee, D.-Y., and Cho, K.-J. (2019). Bioinspired dual-morphing stretchable origami. Sci. Robot. *4*, eaay3493.

18. Vasios, N., Gross, A.J., Soifer, S., Overvelde, J.T.B., and Bertoldi, K. (2020). Harnessing viscous flow to simplify the actuation of fluidic soft robots. Soft Robot. *7*, 1–9.

19. Jeong, H.B., Kim, C., Lee, A., and Kim, H.-Y. (2023). Sequential multimodal morphing of single-input pneu-nets. Soft Robot. *10*, 1137–1145.

20. Kotikian, A., McMahan, C., Davidson, E.C., Muhammad, J.M., Weeks, R.D., Daraio, C., and Lewis, J.A. (2019). Untethered soft robotic matter with passive control of shape morphing and propulsion. Sci. Robot. *4*, eaax7044.

21. Hao, X.P., Xu, Z., Li, C.Y., Hong, W., Zheng, Q., and Wu, Z.L. (2020). Kirigami-Design-Enabled hydrogel multimorphs with application as a multistate switch. Adv. Mater. *32*, 2000781.

22. Jin, L., Forte, A.E., Deng, B., Rafsanjani, A., and Bertoldi, K. (2020). Kirigami-inspired inflatables with programmable shapes. Adv. Mater. *32*, 2001863.

23. Melancon, D., Gorissen, B., García-Mora, C.J., Hoberman, C., and Bertoldi, K. (2021). Multistable inflatable origami structures at the metre scale. Nature *592*, 545–550.

24. Rafsanjani, A., Zhang, Y., Liu, B., Rubinstein, S.M., and Bertoldi, K. (2018). Kirigami skins make a simple soft actuator crawl. Sci. Robot. *3*, eaar7555.

25. Zhai, Z., Wu, L., and Jiang, H. (2021). Mechanical metamaterials based on origami and kirigami. Appl. Phys. Rev. *8*, 041319.

26. Overvelde, J.T.B., Weaver, J.C., Hoberman, C., and Bertoldi, K. (2017). Rational design of reconfigurable prismatic architected materials. Nature *541*, 347–352.

27. Li, Y., and Yin, J. (2021). Metamorphosis of three-dimensional kirigami-inspired reconfigurable and reprogrammable architected matter. Mater. Today Phys. *21*, 100511.

28. Li, Y., Di Lallo, A., Zhu, J., Chi, Y., Su, H., and Yin, J. (2024). Adaptive hierarchical origami-based metastructures. Nat. Commun. *15*, 6247.

29. Jones, T.J., Jambon-Puillet, E., Marthelot, J., and Brun, P.-T. (2021). Bubble casting soft robotics. Nature *599*, 229–233.

30. Gorissen, B., Reynaerts, D., Konishi, S., Yoshida, K., Kim, J.-W., and De Volder, M. (2017). Elastic inflatable actuators for soft robotic applications. Adv. Mater. *29*, 1604977.

31. Tang, Y., Chi, Y., Sun, J., Huang, T.-H., Maghsoudi, O.H., Spence, A., Zhao, J., Su, H., and Yin, J. (2020). Leveraging elastic instabilities for amplified performance: Spine-inspired high-speed and high-force soft robots. Sci. Adv. *6*, eaaz6912.

32. Rothemund, P., Ainla, A., Belding, L., Preston, D.J., Kurihara, S., Suo, Z., and Whitesides, G.M. (2018). A soft, bistable valve for autonomous control of soft actuators. Sci. Robot. *3*, eaar7986.

33. Tang, Y., and Yin, J. (2018). Design of multifunctional soft doming actuator for soft machines. Adv. Mater. Technol. *3*, 1800069.

34. Gorissen, B., Melancon, D., Vasios, N., Torbati, M., and Bertoldi, K. (2020). Inflatable soft jumper inspired by shell snapping. Sci. Robot. *5*, eabb1967.

35. Pal, A., Goswami, D., and Martinez, R.V. (2020). Elastic energy storage enables rapid and programmable actuation in soft machines. Adv. Funct. Mater. *30*, 1906603.

36. Drotman, D., Jadhav, S., Sharp, D., Chan, C., and Tolley, M.T. (2021). Electronics-free pneumatic circuits for controlling soft-legged robots. Sci. Robot. *6*, eaay2627.

37. Chi, Y., Hong, Y., Zhao, Y., Li, Y., and Yin, J. (2022). Snapping for high-speed and high-efficient butterfly stroke–like soft swimmer. Sci. Adv. *8*, eadd3788.

38. Pal, A., Restrepo, V., Goswami, D., and Martinez, R.V. (2021). Exploiting mechanical instabilities in soft robotics: control, sensing, and actuation. Adv. Mater. *33*, 2006939.

39. Cianchetti, M., Laschi, C., Menciassi, A., and Dario, P. (2018). Biomedical applications of soft robotics. Nat. Rev. Mater. *3*, 143–153.

40. Faber, J.A., Udani, J.P., Riley, K.S., Studart, A.R., and Arrieta, A.F. (2020). Dome-patterned metamaterial sheets. Adv. Sci. *7*, 2001955.

41. Melancon, D., Forte, A.E., Kamp, L.M., Gorissen, B., and Bertoldi, K. (2022). Inflatable origami: Multimodal deformation via multistability. Adv. Funct. Mater. *32*, 2201891.

42. Rahman, S., Wu, L., Elmi, E., and Pasini, D. (2023). Zero-power shape retention in soft pneumatic actuators with extensional and bending multistability. Adv. Funct. Mater. *33*, 2304151.

43. Pezzulla, M., Stoop, N., Steranka, M.P., Bade, A.J., and Holmes, D.P. (2018). Curvature-induced instabilities of shells. Phys. Rev. Lett. *120*, 048002.

44. van der Heijden, A.M.A. (2018). W. T. Koiter's Elastic Stability of Solids and Structures (Cambridge University Press).

45. Holmes, D.P., Lee, J.-H., Park, H.S., and Pezzulla, M. (2020). Nonlinear buckling behavior of a complete spherical shell under uniform external pressure and homogeneous natural curvature. Phys. Rev. E *120*, 023003.

46. Taffetani, M., Jiang, X., Holmes, D.P., and Vella, D. (2018). Static bistability of spherical caps. Proc. R. Soc. A A. *474*, 20170910.

47. Lee, A., Jiménez, F.L., Marthelot, J., Hutchinson, J.W., and Reis, P.M. (2016). The geometric role of precisely engineered imperfections on the critical buckling load of spherical elastic shells. J. Appl. Mech. *83*, 111005.

48. Ki, K., Lee, J., and Lee, A. (2024). Combined influence of shallowness and geometric imperfection on the buckling of clamped spherical shells. J. Mech. Phys. Solid. *185*, 105554.

49. Gu, G., Zou, J., Zhao, R., Zhao, X., and Zhu, X. (2018). Soft wall-climbing robots. Sci. Robot. *3*, eaat2874.

50. Liao, B., Zang, H., Chen, M., Wang, Y., Lang, X., Zhu, N., Yang, Z., and Yi, Y. (2020). Soft rod-climbing robot inspired by winding locomotion of snake. Soft Robot. *7*, 500–511.

51. Park, J.-S., Kim, J., Lee, A., and Kim, H.-Y. (2023). Snap-through inversion of elastic shells swelling via solvent diffusion. Soft Matter *19*, 8213–8220.

52. Chi, Y., Li, Y., Zhao, Y., Hong, Y., Tang, Y., and Yin, J. (2022). Bistable and multistable actuators for soft robots: Structures, materials, and functionalities. Adv. Mater. *34*, 2110384.

53. Xavier, M.S., Tawk, C.D., Zolfagharian, A., Pinskier, J., Howard, D., Young, T., Lai, J., Harrison, S.M., Yong, Y.K., Bodaghi, M., and Fleming, A.J. (2022). Soft pneumatic actuators: A review of design, fabrication, modeling, sensing, control and applications. IEEE Access *10*, 59442–59485.

54. Van Raemdonck, B., Milana, E., De Volder, M., Reynaerts, D., and Gorissen, B. (2023). Nonlinear inflatable actuators for distributed control in soft robots. Adv. Mater. *35*, 2301487.

55. van Laake, L.C., de Vries, J., Malek Kani, S., and Overvelde, J.T. (2022). A fluidic relaxation oscillator for reprogrammable sequential actuation in soft robots. Matter *5*, 2898–2917.

56. Klute, G.K., Czerniecki, J.M., and Hannaford, B. (1999). McKibben artificial muscles: pneumatic actuators with biomechanical intelligence. In IEEE/ASME International Conference on Advanced Intelligent Mechatronics (IEEE), pp. 221–226.

57. Kim, S.Y., Baines, R., Booth, J., Vasios, N., Bertoldi, K., and Kramer-Bottiglio, R. (2019). Reconfigurable soft body trajectories using unidirectionally stretchable composite laminae. Nat. Commun. *10*, 3464.

Supplemental information

Snap inflatable modular metastructures

for multipath, multimode morphing machines

Ji-Sung Park, Kanghyun Ki, Anna Lee, Jeong-Yun Sun, and Ho-Young Kim

NOTE S1. ANALYSIS OF SNAP-FOLDING ANGLE

The snap-folding angle α presented in the main text can be obtained as follows. We start by assuming that the shells minimally deform due to the presence of neighbouring cells. To validate this assumption, we reference the classical analytical solutions by Pogorelov, which predict significant nonlinear indentations in thin, spherical shells subjected to concentrated point forces.[1] Specifically, the non-dimensionalized indentation depth ξ relative to the shell thickness h is given by

$$\frac{\xi}{h} = \frac{1}{9\pi^2 c^2} \left(\frac{R}{h}\right)^2 \left(\frac{F}{Eh^2}\right)^2, \tag{S1}$$

where $c = 0.19$ is a numerical coefficient, and the formula applies to deep shells as long as the deformation remains localized in shallow regions.[2]

From Eq. (S1), it becomes clear that shells with rather larger thickness h and a lower slenderness ratio $\eta = R/h$ are less likely to deform under external point loads. For a typical shell used in our experiments with parameters $h = 10^{-3}$ m, $\eta = 6$, $E = 10^6$ Pa, an external force required to indent the shell by its own thickness ($\xi = h$) would be:

$$F = 3\pi cEh^2 \sqrt{\frac{\xi}{h}} \left(\frac{h}{R}\right) = 3(\pi)(0.19)(10^6)(10^{-3})^2(1)(1/6) = 0.30 \text{ N}. \tag{S2}$$

Thus, a single shell can withstand a load of about 0.03 kg without indenting more than 1 mm, which is sufficiently greater than the 0.01 kg weight per module, including auxiliary pneumatic parts, used in our demonstrations. In addition, magnets embedded on the lateral sides of each cell assist in aligning the shells for each mode, with an attractive force of less than 0.5 N–precisely calibrated to avoid interfering with the transformations, depending on the design. This helps reduce the load on shell surfaces even when the robots assume configurations where cells press against each other.

Therefore, we proceed by deriving the snap-folding angle based solely on the geometrical relations. To simplify the analysis, as guided by experimental observations, we approximate the profile of a post-snapped shell to be the same as the pre-snap shell, with the addition of a cylindrical base of height h (Fig. 2B and S3A). For this assumption to be valid, the distance of the apex from the rim support of snapped shell, H, should to be equal to $H_0 + h$, where H_0 is the height of the apex measured from the rim support of the initial pre-snap shell. From geometrical relations, $H_0 = (R + h/2)(1 - \cos\theta)$. Comparing the experimental and computational results of H with initial pre-snap height H_0, we observe the relation $H = H_0 + h$, thereby validating the model for the profile of the post-snapped shell (Fig. S3B). By utilizing this simplified geometrical representation of a post-snapped shell, we obtain the analytical expression for α.

We denote the center point of the spherical cap as **O** and project it onto the imaginary upper surface of rim support to obtain point **S**. The folding hinge point and shell contact point are denoted as **F** and **C**, respectively (Fig. S3A). Then the snap-folding angle is twice the sum of the two angles $\alpha = 2(\angle\textbf{OFS} + \angle\textbf{OFC})$. As the length of $\overline{\textbf{OS}}$ is $H - R - \frac{h}{2}$, the length of $\overline{\textbf{OF}} = \sqrt{\overline{\textbf{OS}}^2 + \overline{\textbf{SF}}^2}$ is $\sqrt{L^2 + (H - R - h/2)^2}$. Therefore, $\overline{\textbf{CF}} = l = \sqrt{L^2 + (H - R - h/2)^2 - (R + h/2)^2}$. Summing up the angle of the two triangles, we obtain:

$$\alpha = 2\left\{\tan^{-1}\left[\frac{R + \frac{h}{2}}{\sqrt{L^2 + (H - R - \frac{h}{2})^2 - (R + \frac{h}{2})^2}}\right] + \tan^{-1}\left(\frac{H - R - \frac{h}{2}}{L}\right)\right\}. \tag{S3}$$

By non-dimensionalizing the length parameters using the shell radius R, the snap-folding angle is given as in the main text:

$$\alpha = 2\left\{\tan^{-1}\left[\frac{\beta}{\sqrt{\hat{L}^2 + \left(\hat{H} - \beta\right)^2 - \beta^2}}\right] + \tan^{-1}\left[\frac{1}{\hat{L}}\left(\hat{H} - \beta\right)\right]\right\}. \tag{S4}$$

Fig. S3C shows that our analytical predictions are consistent with the experimentally and computationally obtained α for various shells with $1 < \hat{H} < 3$ and $0.1 < \hat{h} < 0.5$.

NOTE S2. SUPPORTING THEORY FOR SNAP-THROUGH PRESSURE

We provide supporting theory for the scaling analysis of snap-through pressure presented in the main text. We first divide the rim-clamped shells into two distinct regions: spherical shell and rim support, to calculate the energy accumulated by changes in curvature. The potential energy of shell region, Π_κ, induced by curvature κ again decouples into bulk and boundary terms $\Pi_\kappa = -W_{\text{bulk}} - W_{\text{edge}}$.[3] Each term reads

$$W_{\text{bulk}} = -\frac{Eh}{8(1-\nu^2)}\frac{4(1+\nu)}{3}\left(\frac{h}{R}\right)^2 \kappa \int \Psi_3 \, \mathrm{d}w \tag{S5}$$

and

$$W_{\text{edge}} = \frac{Eh}{8(1-\nu^2)}\frac{2(1+\nu)}{3}h^2\kappa \oint \left(\vec{q} - \frac{\check{\vec{\Psi}}}{R}\right)\cdot\vec{t}\,\mathrm{d}s. \tag{S6}$$

We also consider the strain energy of rim support, U_{p}, using Koiter's classical shell energy to scale stretching and bending terms as $U_{\text{p}} = U_{\text{s}} + U_{\text{b}} \sim Et/(1-\nu^2)\int_A \epsilon_{\text{p}}^2\,\mathrm{d}w + Et^3/[12(1-\nu^2)]\int_A \kappa_{\text{p}}^2\,\mathrm{d}w$, where ϵ_{p} and κ_{p} are strain and curvature of rim, respectively. With the expressions of four energy components W_{bulk}, W_{edge}, U_{s}, U_{b}, we compare each component to find the dominant factor of shell deformation.

First, we examine cases where the rim undergoes considerable amount of stretching before the shell starts to deform. Experimental and computational results reveal that for shells with high slenderness ratio ($\eta = R/h \gg 1$), the predominant behaviour before snap-through is the outward bending of the shell edge. For those shells that deviate from the classical shell assumption ($\eta = R/h \sim 1$), the rim support undergoes extensive stretching before the bending of the shell edge occurs. We can rationalize these assumptions by comparing the two scenarios, pure stretching of the rim support without deformation of the shell and pure bending of the rim support with edge bending of the shell. For the former case, where only the rim is stretched, the elastic energy of the system is approximated as $U_{\text{s}} \approx Et/(1-\nu^2)\int_A \epsilon_{\text{p}}^2\,\mathrm{d}w \approx [Et/(1-\nu^2)]\epsilon_{\text{p}}^2 A_{\text{p}}$. For the latter case, shell deformation W_{bulk} and W_{edge} also contribute to the total elastic energy of the system. Using the scaling result of Pezzulla et al[3] and assuming axisymmetric deformation, the two energies are approximated as

$$W_{\text{bulk}} \approx \frac{Eh}{8(1-\nu^2)}\frac{4(1+\nu)}{3}h^4\kappa^2 2\pi(1-\cos\theta), \tag{S7}$$

and

$$W_{\text{edge}} \approx \frac{Eh}{8(1-\nu^2)}\frac{2(1+\nu)}{3}h^4\kappa^2\left(\frac{R}{h}\right)^{\frac{3}{2}}2\pi\sin\theta. \tag{S8}$$

Moreover, the bending energy of rim support is approximated as $U_{\text{b}} \approx \{Et^3/[12(1-\nu^2)]\}\kappa_{\text{p}}^2 A_{\text{p}}$. The ratio of the energies involved in the two scenarios then becomes

$$\Gamma = \frac{W_{\text{bulk}} + W_{\text{edge}} + U_{\text{b}}}{U_{\text{s}}} \approx$$
$$\frac{\frac{Eh}{8(1-\nu^2)}\frac{4(1+\nu)}{3}h^4\kappa^2 2\pi(1-\cos\theta) + \frac{Eh}{8(1-\nu^2)}\frac{2(1+\nu)}{3}h^4\kappa^2\left(\frac{R}{h}\right)^{\frac{3}{2}}2\pi\sin\theta + \frac{Et^3}{12(1-\nu^2)}\kappa_{\text{p}}^2 A_{\text{p}}}{\frac{Et}{1-\nu^2}\epsilon_{\text{p}}^2 A_{\text{p}}}, \tag{S9}$$

where $A_{\text{p}} = (2L)^2 - \pi(R\sin\theta)^2$ is the area of the rim support. At the moment of snap-through, the tangential plane on the shell boundary becomes approximately horizontal, and the critical curvature within the boundary layer scales as $\kappa \sim \theta/\sqrt{Rh}$.[3] This also allows us to assume the rim support as a quadrant of circle with constant curvature

$\kappa_p \sim 1/R_p \sim \pi/(2L - 2R\sin\theta)$. Substituting the relations into Eq. (S9), we obtain

$$\Gamma = \frac{W_{\text{bulk}} + W_{\text{edge}} + U_b}{U_s} \sim$$

$$\left\{ \frac{1}{4\left(\frac{4}{\pi}\left(\frac{L}{R}\right)^2 - \sin^2\theta\right)} \left(\frac{h}{R}\right)^{\frac{3}{2}} \left(\frac{h}{t}\right) \theta^2 \sin\theta \left[\left(\frac{h}{R}\right)^{\frac{3}{2}} \tan\frac{\theta}{2} + 1\right] + \gamma \frac{1}{\left(\left(\frac{L}{R}\right)^2 - \sin\theta\right)^2} \frac{\pi^2}{3} \left(\frac{t}{R}\right)^2 \right\} \frac{1}{\epsilon_p^2}, \tag{S10}$$

where γ is a numerical prefactor of order 1. We see that the snapping of shells with high η, small θ, and high L/R exhibits the ratio $\Gamma \ll 1$, implying the dominant roles of bending of the rim support and shell edge with the effect of rim stretching negligible. When Γ is large, indicating the scenario where the bending contributions are overshadowed by the effect of rim stretching, the behavior of the shells diverges from this bending-dominated mechanism. Fig. S4A replots Fig. 2D, with the symbols coloured according to the energy ratio of Eq. (S10). Indeed, for shells exhibiting a large value of Γ, which are positioned on the right-hand side of the figure and for which $\eta \leq 2$, there is a noticeable deviation from the linear fitting relation derived from the scaling analysis in the main text. As we focus on snapping structures that minimize stretching deformation of rim support (preventing excessive bulging of the folding hinge), the following analyses specifically consider the latter case with lower values of $(h/R)\,\theta$.

Now we compare W_{bulk}, W_{edge}, and U_b to determine which energy dominates for the deformation of the shells of the latter case. Comparing the two energy components within the shell region W_{bulk} and W_{edge},

$$\frac{W_{\text{edge}}}{W_{\text{bulk}}} \sim \frac{(R/h)^{3/2}}{\tan(\theta/2)}, \tag{S11}$$

we find that for the majority of shells within the experimental conditions ($\eta > 1$), W_{edge} dominates over W_{bulk} as illustrated in Fig. S4B. Then, through a comparison of shell edge and rim bending energies

$$\frac{W_{\text{edge}}}{U_b} \sim \frac{\left(\left(\frac{L}{R}\right)^2 - \sin\theta\right)^2}{\left(\frac{L}{R}\right)^2 - \frac{\pi}{4}\sin^2\theta} \frac{3}{\pi} \left(\frac{h}{t}\right)^3 \left(\frac{R}{h}\right)^{\frac{1}{2}} \theta^2 \sin\theta, \tag{S12}$$

we find that shells with high η and large θ would exhibit shell edge dominated snap-through ($W_{\text{edge}}/U_b \gg 1$). Another factor significantly affecting the deformation is the relative thickness of the shell compared to the rim support, h/t. Specifically, when the shell thickness is very thin and comparable to the thickness of the rim (e.g. $h \sim 1$ mm), as shown in the leftmost region of Fig. S4C, the effect of rim bending becomes significant.

Therefore, we conclude that the elastic energy of large, thin shells (but thicker than the rim support), as observed in the intermediate regions of the figure sets ($200 < E/(1-\nu)\,\hat{L}^{-2}\hat{h}\theta\sin\theta < 500$), can be accurately modelled by solely considering the outward bending of the shell boundary. Hence, we proceed to scale the shell boundary work, W_{edge}, and pressure potential, Π_P, as presented in the main text, and determine the critical pressure at snap-through for rim-supported shells:

$$P_s \sim \frac{E}{(1-\nu)} \left(\frac{L}{R}\right)^{-2} \left(\frac{h}{R}\right) \theta\sin\theta \sim \frac{E}{(1-\nu)} \hat{L}^{-2}\hat{h}\theta\sin\theta. \tag{S13}$$

Enhanced scaling can be obtained by incorporating the shell bulk energy neglected above. By scaling Π_P with $W_{\text{edge}} + W_{\text{bulk}}$, modified critical pressure at snap-through for P_s' reads:

$$P_s' \sim \frac{E}{(1-\nu)} \left(\frac{L}{R}\right)^{-2} \left(\frac{h}{R}\right) \theta\sin\theta \left[1 + \left(\frac{h}{R}\right)^{\frac{3}{2}} \tan\theta\right] \sim \frac{E}{(1-\nu)} \hat{L}^{-2}\hat{h}\theta\sin\theta \left(1 + \hat{h}^{\frac{3}{2}}\tan\theta\right). \tag{S14}$$

Fig. S5 shows that the linear fitting of the experimental and computational results to P_s' are slightly improved compared to P_s.

In summary, depending on the geometrical parameters of shell and rim support, the major deformation modes differ. If the shells are too small in radius, thick, and deep, stretching of rim support and shell bulk deformation dominate the system. In contrast, if the shells are too thin, comparable to the thickness of rim support, the effect of bending in the rim support becomes more pronounced. Otherwise, rim-clamped shells exhibit snap-through primarily

dominated by shell boundary-deformation, the scenario employed above.

In our prediction model, we primarily consider axisymmetric deformations where edge bending is dominant, and no prior local buckling occurs. The critical buckling pressure, derived from linear buckling analysis, is given by

$$P_{cr} = \frac{2E}{\sqrt{3\left(1 - \nu^2\right)}} \left(\frac{h}{R}\right)^2, \tag{S15}$$

which establishes the upper limit for the buckling in spherical shells.[4] Comparing this with the snap-through pressure P_s, we find:

$$\frac{P_s}{P_{cr}} \sim \hat{L}^{-2}\hat{h}^{-1}\theta \sin\theta. \tag{S16}$$

This suggests that for shells with high $\hat{L}$ and $\hat{h}$ and low θ, axisymmetric edge bending will predominantly dictate snap-through. If the thin and deep shell is tightly clamped near the edge local buckling will occur and reduce the threshold pressure considerably. Moreover, if the shell has any imperfections, the actual buckling pressure can drop to as low as 20% of P_{cr}, further affecting the phenomenon. A potential solution to address this imperfection could be intentionally implementing controlled defects,[5,6] as discussed in the main text. By designing shells with a significantly large defect ($\delta/h > 0.3$), we can achieve a plateau in buckling threshold reduction. This approach effectively decreases the imperfection sensitivity, ensuring a more robust and predictable snap-through.

Additionally, we have observed the stability of shells through our experimental results. When the shells are too thick, small, and shallow, characterized by a small dimensionless shell parameter $\lambda = \left[12\left(1 - \nu^2\right)\right]^{1/4}\theta\sqrt{R/h}$, the system loses its bistability (Fig. S2C). Utilizing such monostable shells in SIMMs would enable an autonomous snap-back mechanism, albeit with a trade-off in the multistability of the system.

It is important to note that while these effects are acknowledged, our primary focus in this study is on providing intuitive guidance for shell design as soft actuators. Specifically, we concentrate on constructing snap hinges with varying rigidity by modifying material and geometrical parameters of the shells.

NOTE S3. SYSTEMATIC LIBRARY OF MORPHING CONFIGURATIONS

We present an example of constructing a morphing library to systematically organize reconfigurable designs using modular assemblies and the SIMM principle. This methodology facilitates the identification and classification of morphing configurations based on connectivity and hinge placement. For simplicity, the library in Fig. S6 utilizes cubic cells connected by snap hinges with a snap-folding angle of $90°$.

Each design in the library achieves distinct reconfigurations via snap-through folding, determined by the connectivity between pneumatic cells and the placement of snapping shells. The naming format specifies: (1) the interface between cells where the snapping shell is located, and (2) the face where the rotational hinge is attached. As shown in Fig. S6A, face numbers are assigned to each cube face according to a planar map. For instance, the design shown in Fig. S6B, consisting of one snapping shell placed at face 3 of cell A (connected to face 4 of cell B), with the rotational hinge on face 1 of both cells, is denoted as A3-B4-1. Using three pneumatic cells and two distinct snapping shells across the interfaces, eight unique designs with different morphing sequences are identified, as depicted in Fig. S6C. The resulting morphing positions of cell C are tracked in 3D space, with their trajectories represented as colored dots in Fig. S6D.

This library can be further expanded by integrating continuous pneumatic functions into each cell and utilizing computational tools or inverse design methodologies. These advancements could enable the development of more sophisticated and multifunctional systems designed for a wide range of applications.

Materials	Young's Modulus [MPa]
Dragon Skin 10	0.19 ± 0.0059
Dragon Skin 30	0.50 ± 0.015
Smooth-Sil 950	0.76 ± 0.023
Dragon Skin 30: Dragon Skin 10 1:1	0.34 ± 0.012
Dragon Skin 30: Smooth-Sil 950 1:1	0.65 ± 0.035

TABLE S1: Tensile test results of Young's moduli of different silicone-based elastomers and their mixtures.
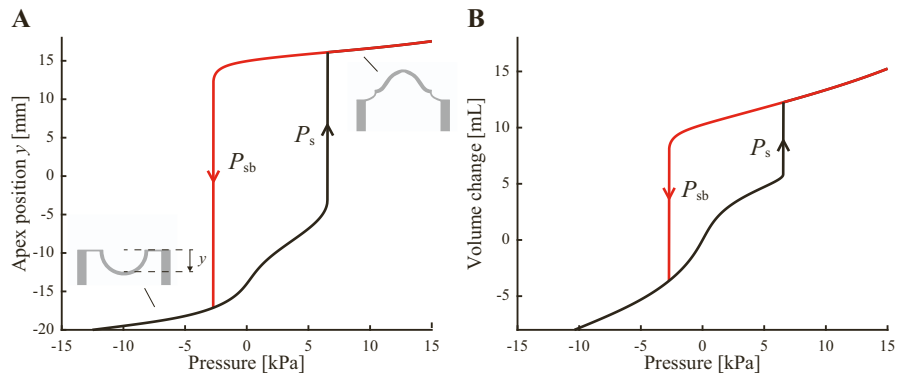
FIG. S1: Snap-through and snap-back transitions of a single snap unit. Computational results showing (A) pressure-apex position curve and (B) pressure-volume change curve for a snap unit with $R = 12$ mm, $h = 2$ mm, $\theta = 90°$, and $L = 20$ mm under cyclic pressurization and depressurization. The snap-through pressure P_s and snap-back pressure P_sb are determined as 6.5 kPa and -2.7 kPa, respectively, corresponding to points of significant volume change.
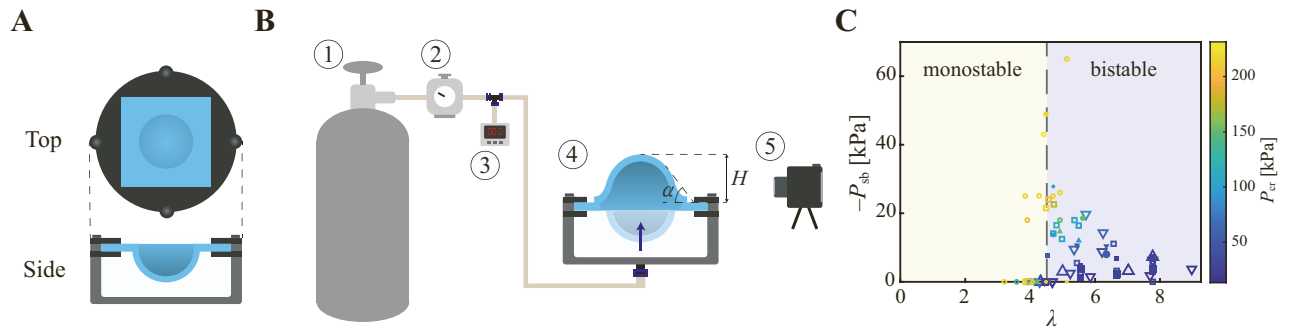
FIG. S2: Snap-through measurement of rim-clamped shells. (A) Top and side view of rim-clamped shell. (B) Experimental set-up for shell snap measurement. 1: Nitrogen gas tank, 2: Pressure regulating valve, 3: Digital pressure gauge, 4: rim-clamped shell, 5: CMOS camera. (C) Experimental and computational result of snap-back pressure versus dimensionless shell parameter $\lambda = \left[12\left(1 - \nu^2\right)\right]^{1/4} \theta \sqrt{R/h}$. The transition from monostable to bistable behavior occurs at $\lambda \sim 4.5$ for the rim-clamped boundary conditions. Symbol colours indicate critical buckling pressure of complete sphere of the same radius R and thickness h, $P_{\mathrm{cr}} = \left\{2E/\left[3\left(1 - \nu^2\right)\right]^{1/2}\right\}(h/R)^2$.
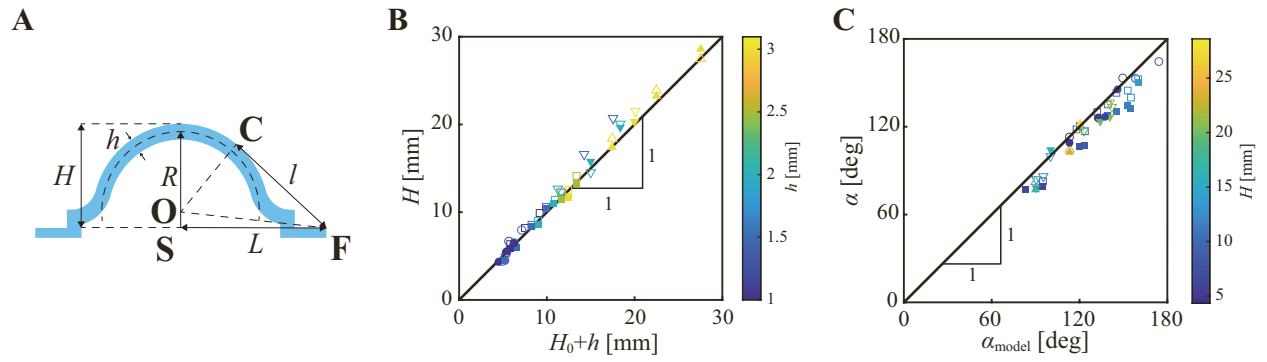
FIG. S3: Determination of folding angle of the SIMM. (A) Schematic illustration of the model for exterior profile of post-snapped shell. (B) Experimentally and computationally measured post-snapped height H compared with $H_0 + h$. Symbol colour indicates shell thickness h. (C) Comparison of experimental and computational results of snap-folding angle α versus analytically obtained α_{model}. The symbol colour indicates snapped height H. Empty symbols and coloured symbols correspond to experimental and computational data, respectively.
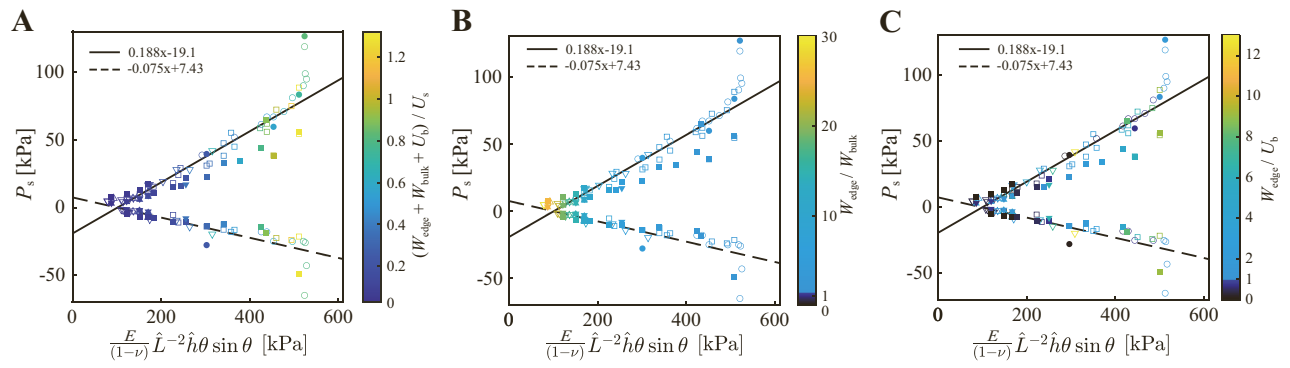
FIG. S4: Snap-through and snap-back pressure with symbols whose colours indicate energies associated with shell deformation. Experimental and computational result of snap-through pressure with the symbol colours indicating energy ratios: (A) $(W_{bulk} + W_{edge} + U_b)/U_s$, (B) W_{edge}/W_{bulk}, and (C) W_{edge}/U_b.
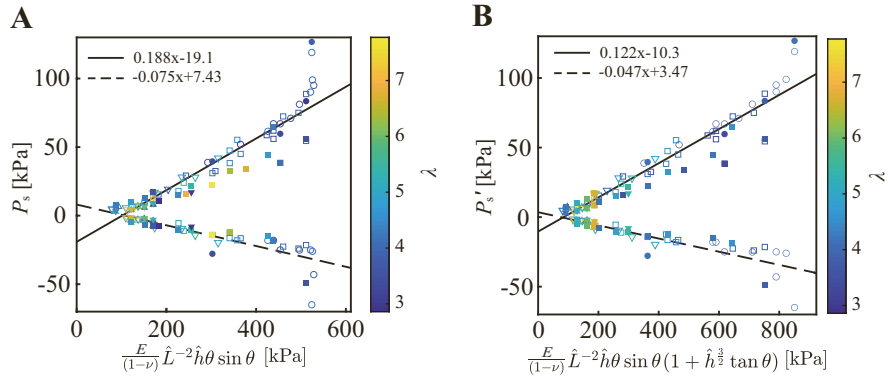
FIG. S5: Comparison of original and modified snap-through pressure. Comparison of (A) pressure scaling P_s obtained by assuming the dominant energy as W_{edge} ($r^2 = 0.86$) and (B) modified scaling P_s' obtained by assuming the dominant energy as $W_{edge} + W_{bulk}$ ($r^2 = 0.91$).
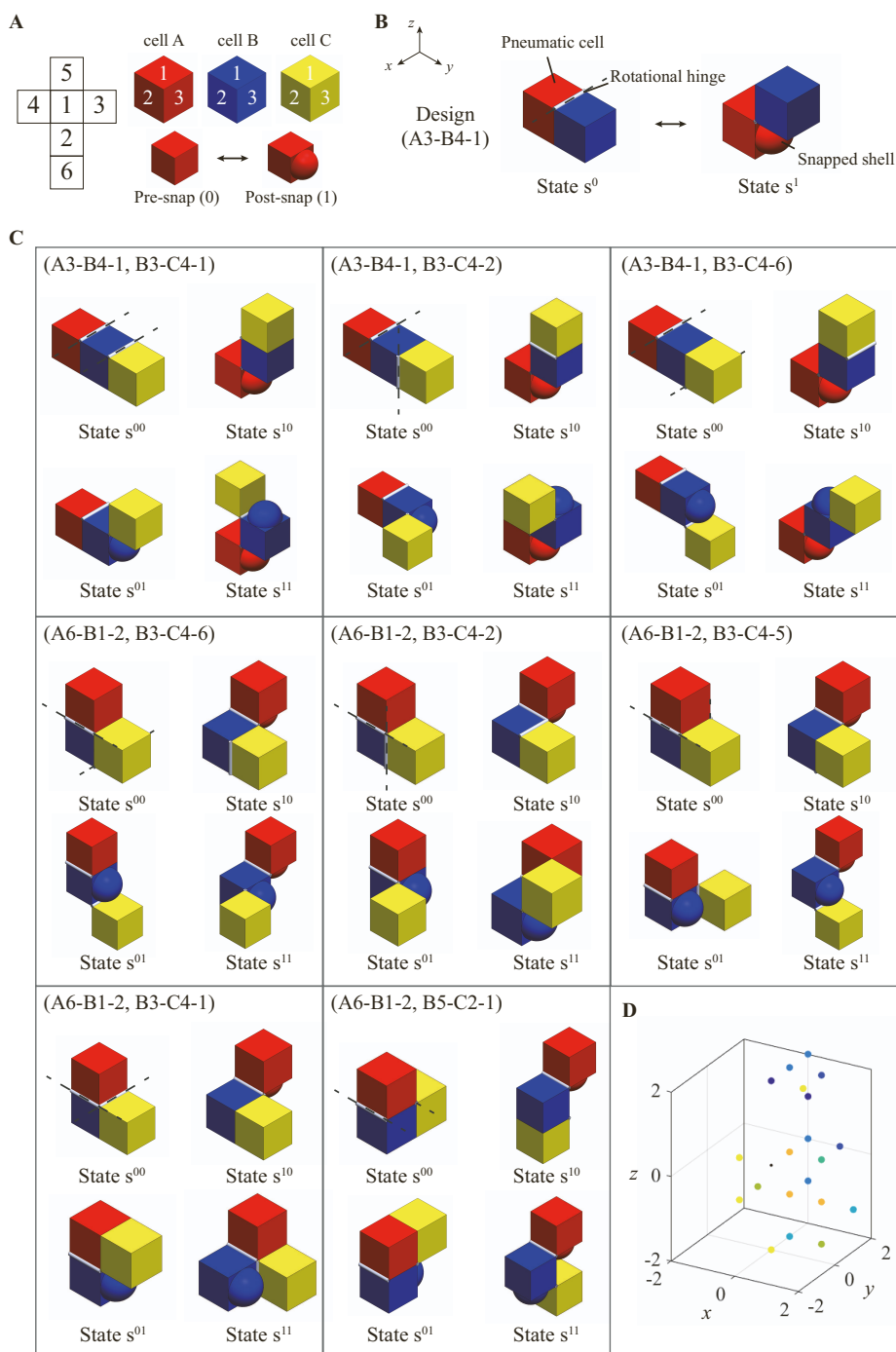
FIG. S6: Example of a systematic library of morphing configurations using cubic cells. (A) A planar mapping assigning numbers to cubic cell faces for systematic identification of snapping and hinge connections. (B) Example design A3-B4-1 consists of two cubic cells, showing a snapping shell at face 3 of cell A (connected to face 4 of cell B) and a rotational hinge at face 1 of both cells, enabling transitions between pre-snap (s^0) and post-snap (s^1) states. (C) Eight unique designs derived from three pneumatic cells and two snapping shells, each showing distinct morphing sequences and configurations. (D) Final morphing positions of cell C tracked in 3D space.
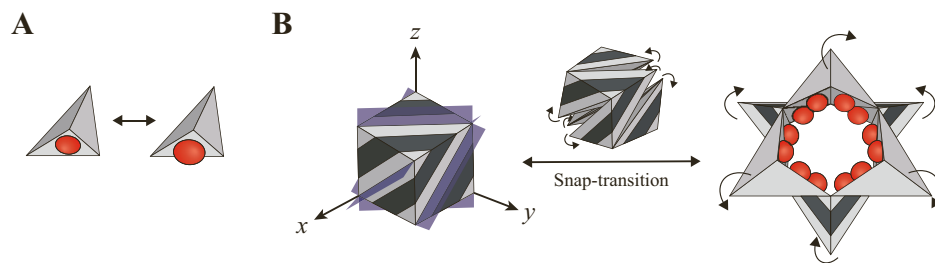
FIG. S7: Morphing pattern of SIMMs using tetrahedral snap unit. (A) Snap-transition of a tetrahedral snap unit having a cap shell on one of its facets. (B) Three-dimensional closed-loop transition from a cubic configuration to a star-shaped configuration using tetrahedral SIMMs.
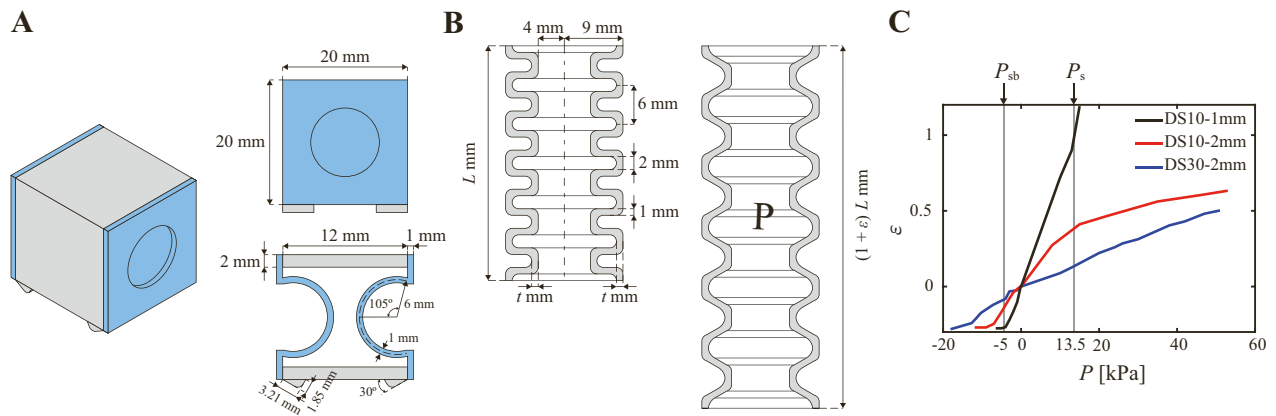
FIG. S8: Characterization of extension-snap module. (A) Design of a cubic snap unit. (B) Geometry and (C) deformation of the bellows-shaped extension actuator. Bellows of the initial length $L = 20$ mm is elongated to $(1 + \epsilon) L$ upon inflation by pressure P. Elastomers, Dragon Skin 10 and Dragon Skin 30, are used to compare elongation with different wall thicknesses $t = 1$ and 2 mm. P_s and P_{sb} indicate shell snap and snap-back pressure of the snap unit, respectively.
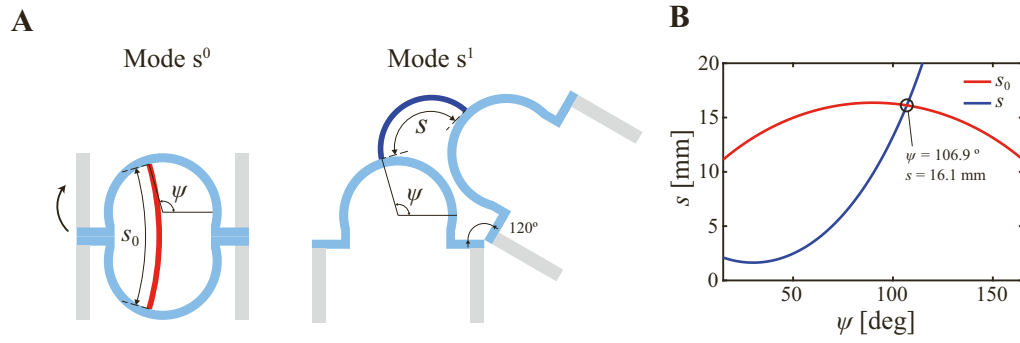
FIG. S9: Design of tendon for spinning ball robot. (A) Geometry of the tendon at pre-snap mode s^0 and post-snapped mode s^1, positioned at meridional angle ψ. (B) Length of the tendon at pre-snap mode, s_0, and at post-snapped mode, s, plotted with ψ. The two tendon lengths are identical as $s = 15.9$ mm when $\psi = 106°$, which is adopted in the robot design.

A

B

2.5 mm
1 mm
20 mm
1 mm
20°
4 mm
45°

Direction of locomotion

C

Mode s^0

Ratchet leg

20 mm

10.6 mm
1 mm
22 mm
Magnet

Mode s^1

R6 mm
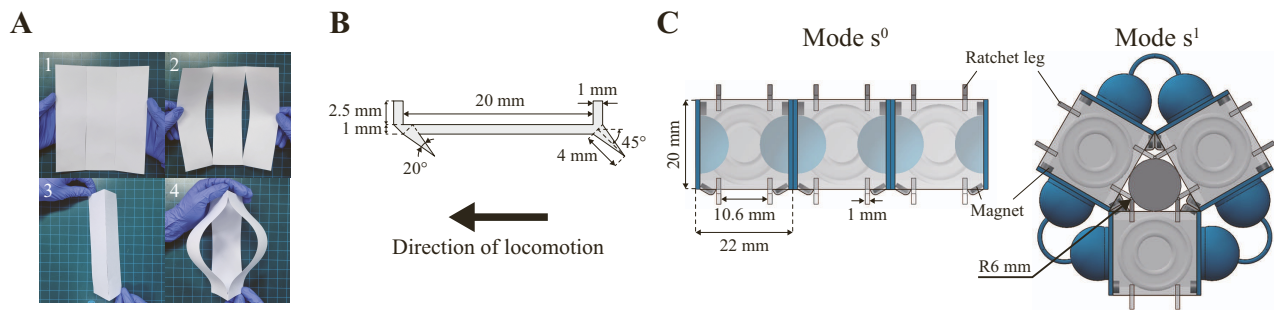
FIG. S10: Design and assembly of spinning ball robot. (A) Design of a three-cell spinning ball origami with two kirigami cuts, fabricated using a sheet of paper. The sequence illustrates the transformation: 1) flat compact state (top-left), 2) flat deployed state (top-right), 3) cylindrical compact state (bottom-left), and 4) cylindrical deployed state (bottom-right). (B) Ratchet leg design of spinning ball robot. The inclined legs enable the robot undergoing periodic lengthwise oscillation to crawl in a rectified fashion. The direction of locomotion is specified with a large black arrow. (C) Front view of ground crawling mode s^0 and cable climbing mode s^1.

A

B
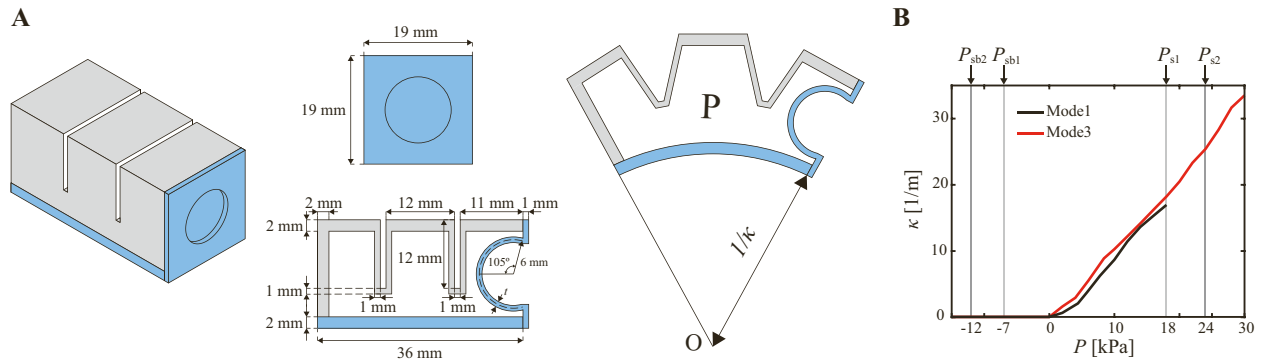
FIG. S11: **Characterization of bending-snap module.** (A) Geometry and (B) deformation of the bending-snap module. The pleated structure on the top bends to curvature κ upon inflation by pressure P. $P_{s,1}$, $P_{s,2}$ and $P_{sb,1}$, $P_{sb,2}$ indicate shell snap and snap-back pressure of shell 1 and shell 2, respectively.
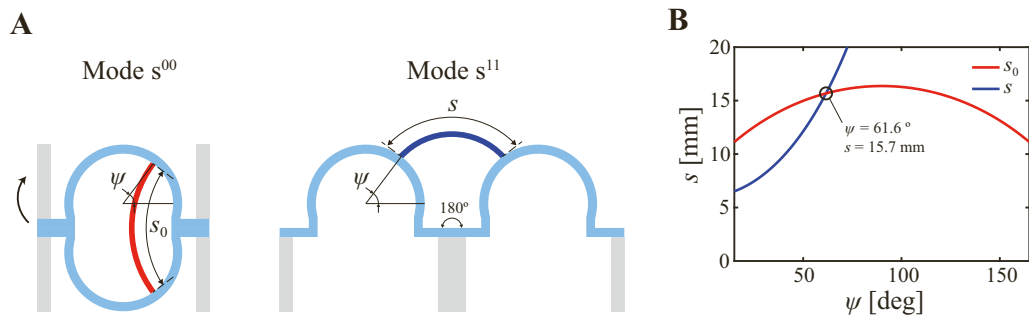
FIG. S12: Design of tendon for quad-tessellation robot. (A) Geometry of tendon of pre-snap and snapped shell positioned at the meridional angle ψ for the design of the quad-tessellation robot. (B) Length of the tendon at pre-snap mode, s_0, and at post-snapped mode, s, plotted with ψ. The two tendon lengths are identical as $s = 14.8$ mm when $\psi = 59°$, which is adopted in the robot design.
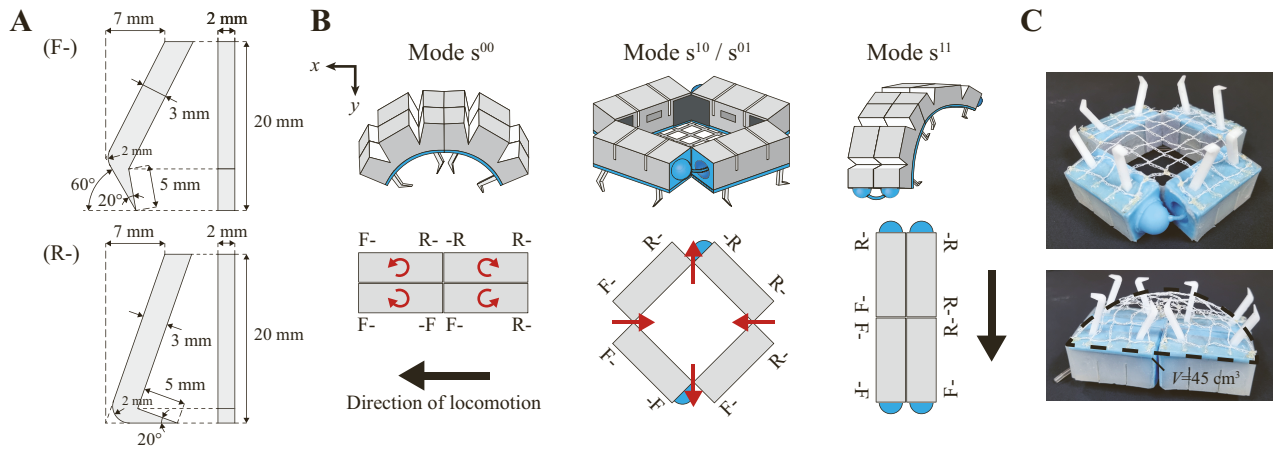
FIG. S13: Design and assembly of quad-tessellation robot. (A) Front (F-) and rear (R-) leg designs of the quad-tessellation robot. Dash sign (-) is used to indicate the alignment of the legs. (B) Orientation of legs to ensure directional locomotion for both x-directionally-aligned closed mode s^{00} and y-directionally-aligned closed mode s^{11}. The direction of locomotion is specified with a large black arrow. (C) Bottom view of the robot. The cargo net encloses an interior volume of $V=45$ cm^3 in its closed mode.

SUPPLEMENTAL REFERENCES

1. Pogorelov, A. V. (1988). Bendings of surfaces and stability of shells. American Mathematical Soc. *72*.

2. Abbasi, A., Yan, D., & Reis, P. M. (2021). Probing the buckling of pressurized spherical shells. J. Mech. Phys. Solids. *155*, 104545 .

3. Pezzulla, M., Stoop, N., Steranka, M. P., Bade, A. J., & Holmes, D. P. (2018). Curvature-induced instabilities of shells. Phys. Rev. Lett. *120*, 048002.

4. Zoelly, R. (1915). Ueber ein Knickungsproblem an der Kugelschale (Ph.D. thesis) (ETH Zürich).

5. Lee, A., Jiménez, F. L., Marthelot, J., Hutchinson, J. W., & Reis, P. M. (2016). The geometric role of precisely engineered imperfections on the critical buckling load of spherical elastic shells. J. Appl. Mech. *83*, 111005.

6. Ki, K., Lee, J., & Lee, A. (2024). Combined influence of shallowness and geometric imperfection on the buckling of clamped spherical shells. J. Mech. Phys. Solids. *185*, 105554.